CHAPTER 4

STRUCTURE AND RHEOLOGY OF FIBER SUSPENSIONS

AARON P. R. EBERLE,[1,2] KEVIN ORTMAN,[2] and DONALD G. BAIRD[2]

[1] NIST Center for Neutron Research, National Institute of Standards and Technology, Gaithersburg, MD, USA
[2] Department of Chemical Engineering, Virginia Polytechnic Institute and State University, Blacksburg, VA, USA

CONTENTS

113

4.1 INTRODUCTION

Polymer composites, protective coatings, membranes, ceramics, and structural materials are examples of a diverse class of fiber composites whose precursors are multicomponent fluids consisting of various disperse solids and a continuous phase, the suspending medium. Control of the fiber microstructure and bulk flow properties of the suspensions is vital to the optimization of most manufacturing processes. Hence the rheological behavior and its connection to the suspension microstructure is of technical importance.

In this chapter we review the rheological properties and the connection between rheology and microstructure of fiber suspensions. This does not include nanocomposites or natural fiber composite materials, which are covered in detail in separate chapters. Still, this field is extensive and so we limit the discussion to the major topics and general behaviors of bicomponent fluids consisting of discontinuous and homogeneously dispersed fibers in a suspending medium. This chapter includes the current theoretical treatment of both short and long fibers, and Newtonian and non-Newtonian suspending media. In addition, the chapter discusses the experimental rheological behavior and its connection to the fiber orientation distribution. Additional detail regarding the

experimental rheology can be found in the works of Eberle et al. [1], Zirnsak et al. [2], and Larson [3], while the theory can be found in Chung and Kwon [4], Advani and Tucker [5], and Petrie [6].

The chapter is organized to first give the reader a brief background in specific areas deemed necessary to the concepts discussed here, which include suspension classification and experiments. Then the rheology of rigid fiber suspensions is discussed, followed by flexible fibers. The separation of rigid and flexible fiber suspensions reflects the dramatic differences in both the experimental behavior and approaches to modeling.

4.2 BACKGROUND

The topics discussed in this chapter are complex, and the reader is assumed to have a basic understanding of rheology. To minimize confusion the rheological material functions will be defined following that of the official nomenclature for the Society of Rheology as they are discussed in detail elsewhere [7]. On the other hand, the description of fiber suspensions and the instrumentation used to characterize their behavior directly relates to the interpretation of the rheology. Hence an accurate classification of materials and rheometric devices is needed to delineate the contributing factors to the rheological behavior from both an experimental and numerical perspective. In the subsequent Sections we address this by classifying fiber suspensions by their concentration and length as it relates to flexibility. An important aspect of this work is relating the rheological behavior to the microstructure, which is not a trivial task in fiber suspensions where large diameters and opaque matrices prevent the use of scattering techniques. As a result the current approaches to orientation analysis are included. This is followed by a review of the different rheometers and rheometer geometries commonly used, including a discussion of their strengths and weaknesses with respect to obtaining accurate measurements.

Fibers longer than about 1 μm or so will settle as a result of gravity unless the density of the fluid is matched to that of the particle. An approximation for the sedimentation time, t_s, of a cylinder in a viscous fluid was proposed by Chaouche and Koch [8] in which $t_s = 8\eta_s L / \Delta \rho g d^2 [\ln(2a_r) - 0.72]$ where η_s is the suspending medium viscosity, L is the fiber length, $\Delta \rho$ is the difference in densities, g the acceration due to gravity, d is the fiber diameter, and a_r is the fiber aspect ratio defined as $a_r \equiv L/d$. From this simple expression it is shown that t_s is directly proportional to η_s which conveniently minimizes the effect of sedimentation in most composite fluids discussed here. Therefore, the reader can assume that the contribution of sedimentation to changes in the fiber microstructure is negligible unless otherwise specified.

Brownian motion refers to the random movement of any sufficiently small particle as a result of the momentum transfer from suspending medium molecules. The relative effect that Brownian motion may have on orientation, of anisotropic particles, in a dynamic system can be estimated using the rotary

Peclet number, $Pe \equiv \dot{\gamma}/D_{ro}$ where $\dot{\gamma}$ is the shear rate, and D_{ro} rotary diffusivity, which defines the ratio of the thermal energy in the system to the resistance to rotation. Doi and Edwards [9] estimate $D_{ro} = 3k_BT[\ln(a_r) - \Omega]/\pi\eta_sL^3$, where k_{B} is Boltzmann's constant, T is temperature, and α is a constant in which $\Omega = 0.8$ is a good estimate [10]. Using the scaling argument that when $Pe \gg 1$ Brownian effects can be neglected, which in general is true for particles whose longest dimension is $\geq 10 \, \mu m$ [3]. In the following sections the fiber suspensions can be considered non-Brownian, unless stated otherwise, and as such, the numerical analysis of these systems will not include any Brownian terms. The reader is referred to the works of Doi and Edwards [9] on the dynamics of Brownian rods if interested in such topics.

4.2.1   Fiber Suspension Classification

As discussed later, the dynamic behavior of fiber can be highly dependent on the concentration, and fiber characteristics such as length and flexibility. In this Section we seek to separate fiber suspensions based on their degree of inter-action and flexibility with respect to the applied shear stress. While concentration, length, and flexibility lead to specific classifications, polydispersity is characterized using common statistical averages such as the number average, L_n, and weight average, L_w, and as such will not be discussed.

4.2.1.1   Concentration   Fiber suspensions are typically classified into three concentration regimes: dilute, semidilute, and concentrated, which are based on their volume fraction, $\phi = \pi nL^3/4a_r^2$ where n is the number of fibers per unit volume. The dilute regime is such that the fibers within the suspension are free to both rotate and translate without hydrodynamic interaction or direct contact. Theoretically, this occurs when the average distance between the center of mass of two fibers is greater than L, leading to the constraint of $n < 1/L^3$ or $\phi < a_r^{-2}$. The transition to semidilute occurs just above the dilute upper limit. Here hydrodynamic interaction is the predominant phenomenon with little fiber contact. However, the suspension orientation state is not subject to geometric constraints, which can constrict orientation states. Interaction between fibers becomes theoretically possible for homogeneously dispersed fibers when $n > 1/L^3$ but when the mean spacing between fibers, S_{m}, is on the order of the fiber diameter, physical contact becomes an increasingly significant phenomenon. Therefore, the upper limit is subject to the constraint $S_{\mathrm{m}} \gg d$ [9]. The mean spacing between fibers is a function of the orientation state of the fibers within the suspension. For a random orientation state the mean spacing is estimated as $S_m \cong 1/(nL^2)$ and for a suspension whose fibers are completely aligned the mean spacing is of the order $S_m \cong (nL)^{-1/2}$ [11]. This leads to two upper limits: $n \ll 1/(dL^2)$ for random and $n \ll 1/(d^2L)$ for aligned orientation.

The concentrated regime is where $n \geq 1/(d^2L)$ or $\phi \geq a_r^{-1}$. In this range, the dynamic properties of the fibers can be severely affected by fiber–fiber interactions and can lead to solid-like behavior [12]. It is interesting to note

that most fiber composites of industrial interest typically have fiber concentrations of $\phi > 0.1$ and fall within the concentrated regime. The concentration regimes follow the theories for molecular rods, as, for example, described in Doi and Edwards [9]. In addition to the three regimes defined above, molecular theories define a critical concentration in which molecules will preferentially align and become nematic similar to a phase transition. However, it has yet to be proven that fiber suspensions will also go through this transition.

4.2.1.2 Flexibility Fiber suspensions continuously evolve as the demand for high performance, lightweight, and cost-effective parts drive the development of new materials. Glass, carbon, nylon, Kevlar®, and Nomex® are examples of fibers that have been used to reinforce polymers leading to a wide range of fiber composites with varying properties. While it is reasonable to assume that the rheology of fiber suspensions, regardless of composition, should follow defined trends, in reality, it depends on the flexibility of the fiber with respect to the applied shear stress. This will be discussed in detail later for both the experimental rheology and, perhaps more important, in the section describing the approaches to simulating fiber suspensions.

Within this text the term *flexibility* will be used to describe how stiff a fiber behaves in the presence of flow. In this context, a fiber exhibiting a larger degree of flexibility is easier to bend within a specified flow field. The flexibility of a fiber commonly leads to two classes of materials, short and long. Short fiber suspensions are defined as those that remain rigid within a specified shear field, while long fiber suspensions consist of fibers that flex or bend. Switzer and Klingenberg [13] characterized the flexibility of a fiber using an effective stiffness (S^{eff}) dimensionless number defined as

$$S^{\text{eff}} \equiv \frac{E_Y \pi}{4\eta_s \dot{\gamma} a_r{}^4} \tag{4.1}$$

where E_Y is the Young's modulus, and η_s is the suspending medium viscosity. From this expression, the flexibility of a fiber can be seen to increase with aspect ratio for a material with a given Young's modulus.

4.2.2 Microstructure Analysis

Direct measurement of fiber orientation is a key development used to establish structure−property relationships and test advances in constitutive theory. However, the measurement of fiber orientation within a suspension in its molten or consolidated state is a complex task, especially since the orientation can vary considerably through the thickness of the sample. Current methods used to quantify the orientation include transmission optical microscopy [14], contact microradiography [15], scanning acoustic microscopy [16], scanning electron microscopy [17], nuclear magnetic resonance (NMR) imaging [18], X-ray tomographical imaging [19], and reflection microscopy [20]. Many of these

techniques offer different strengths but have similar weaknesses with image resolution and effective sampling size. Transmission optical microscopy, contact microradiography, and scanning acoustic microscopy provide only two-dimensional images, typically with poor resolution [21]. An automated approach has yet to be developed that incorporates the imaging ability of scanning electron microscopy, NMR imaging, and X-ray tomography [22], which reduces the sample size that can be measured. Reflection microscopy has become the most popular and widely used method. Though it is not clear when the ideas for this method were developed, it is known that its foundation stems from simple geometric analysis of ellipsoids and was directly used to quantify fiber orientation by Darlington and McGinley [15] as early as 1975. This method suffered from the same insufficiencies in being able to process large sample sections to acquire accurate orientation distributions until the advent of economical, high-speed, image analysis systems [23, 24].

In reflection microscopy a section of the sample is cut, often normal to the flow direction, encapsulated in an epoxy resin and polished to a smooth surface. The epoxy prevents the degradation of the fibers at the edge of the sample. Contrast between the matrix and the fiber is produced by oxygen plasma etching; this process creates a rough surface around the fibers, which appear dark in reflected light [22]. The three-dimensional orientation is then calculated from the ellipse that appears at the intersection of a plane.

The orientation of each fiber can be described using a unit vector, **u**, along the backbone of the fiber. The zenith and azimuthal angles θ, φ, respectively, defining the components of **u** for a each fiber can be calculated based on the ratio of the minor m and major M axis and depends on which plane is being processed (4.2); the other angle can be measured directly from the image [5]. Figure 4.1a depicts the elliptical foot print in the $x_1 - x_2$ plane and the angle φ measured directly from the image.
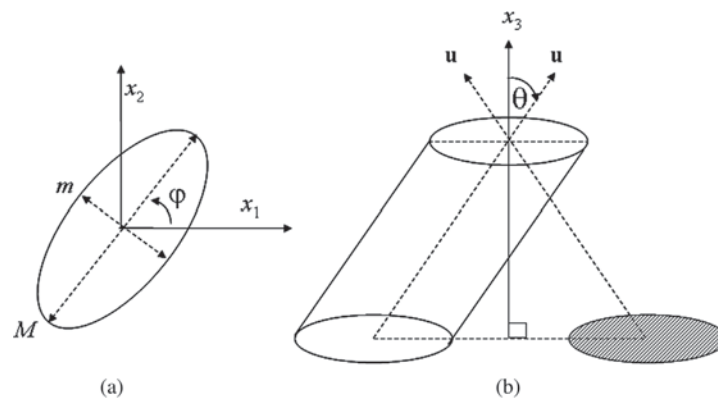
FIGURE 4.1   Fiber orientation angles φ, and θ determined from the elliptical projection [22]. Reprinted with permission from Ref. 26.

$$\cos\theta|_{1-2} = \frac{m}{M}, \ \cos\varphi|_{2-3} = \frac{m}{M} \qquad (4.2)$$

The subscript $1-2$ or $2-3$ refers to the plane being processed. The limitation of calculating the angle based on (4.2) is that the calculated angle is always between 0 and π causing an inherent ambiguity. For example, in the x_1-x_2 plane it is impossible to distinguish between a fiber that is oriented (θ_1, φ_1) and $(\pi - \theta_1, \varphi_1)$ because their cross-sections are identical. Figure 4.1b depicts two possible unit vectors **u** for the same elliptical footprint. Recently, Lee et al. [26] and Eberle et al. [25] used confocal laser microscopy to view the footprints of fiber cross-sections at two planes. This reduced the ambiguity of the technique.

Additional limitations to this method include the many assumptions that are made regarding the distribution of fiber lengths and fiber orientations when correction factors for counting bias are applied [27, 28]. Also, the technique is limited to short fiber composites due to increased and incalculable errors associated with fibers that are not perfectly straight [21]. In the case of long fibers, no dedicated assessment protocol has been identified in literature [29]. Techniques such as X-ray tomography have the ability to capture the 3D spatial distribution, but currently there is no analysis software capable of quantifying the orientation.

4.2.3 Rheometry Flow Field and Boundary Effects

Throughout the literature many different shear rheometers have been used to measure the rheological material functions of fiber suspensions. This includes torsional, capillary, sliding plate, concentric cylinder, falling ball, and Couette. A complete review and mathematical description of the flow field and design equations for each geometry can be found in Macosko [30]. By far the most widely used for polymer composites are the torsional, and capillary rheometers. Traditionally, these types of rheometers were designed to measure the rheology of homogeneous fluids in which case small gaps and capillaries were part of the design criteria to minimize sample volume and velocity field inhomogeneities. For fiber suspensions this represents possible sources of error through fiber-boundary interactions and flow field complications associated with curvilinear streamlines, inhomogeneous flow fields, and particle migration during testing. Subsequently, we briefly discuss both torsional and capillary rheometers in relation to measuring the rheology of fiber suspensions for the primary purpose of informing the reader of possible sources of error that are not easily corrected for.

Torsional rheometers are commonly used to measure the low shear rate $\dot{\gamma} < 10 \ \text{s}^{-1}$, steady-state, and transient rheology. While many fixture designs and geometries are available the cone-and-plate or parallel-disk fixtures are the most commonly used. The cone-and-plate geometry provides a homogeneous shear field but has a small gap of < 0.1 mm near the center and does not allow for gap control. Boundary interactions can occur when the rheometer gap is small

compared to the characteristic length of the filler [31]. For a fiber, the characteristic length can significantly change, depending on its orientation. For instance, a fiber whose orientation is in the shear direction has a characteristic length that is equal to the length of the fiber, while a fiber that is aligned in the flow direction has a characteristic length equal to the diameter of the fiber. To minimize fiber—boundary interaction Blankeney [32] and Attanasio et al. [33] suggested that the sample thickness should be greater than three times the characteristic length of the filler. Boundary interactions are most probable in the case of a fiber tumbling in the shear plane and suppress and broaden the overshoot behavior of the transient material functions [34]. To prevent this Eberle et al. [35] suggested the use of a novel sample geometry in the cone-and-plate geometry where the center of a premolded sample disk was removed, called a *donut sample*, effectively eliminating the region most likely to cause complications due to boundary interaction.

Parallel-disks allow for gap control but the shear rate varies from the center of the plate to the outer edge resulting in an inhomogeneous shear field. Eberle et al. [35] found that that inhomogeneous shear field induces excessive fiber—fiber interaction in concentrated fiber suspensions and can severely affect the magnitude of the stress growth overshoot peak and width of the overshoot. A comparison of the shear stress growth coefficient, η^+, measured using the parallel-disk, and cone-and-plate geometry with and without the donut sample can be seen in Figure 4.2. η^+ measured using the parallel-disk has an exaggerated overshoot and steady-state plateau compared to the cone-and-plate measurements. η^+ measured using the cone-and-plate with unmodified sample
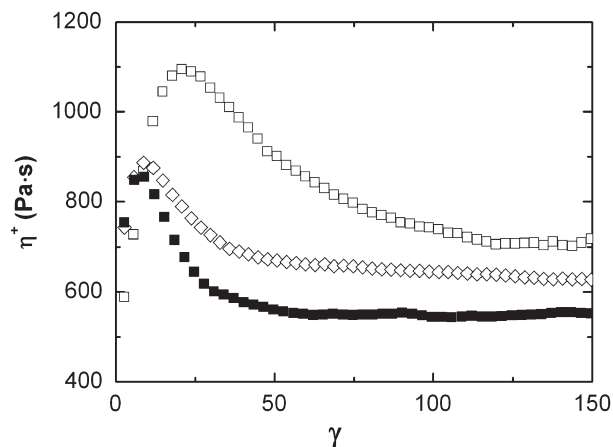
FIGURE 4.2 Stress growth vs. strain in startup of flow measurements for 30 wt % short glass fiber filled polybutylene terephthalate at $\dot{\gamma} = \dot{\gamma}_R = 1 \ s^{-1}$. Shear stress growth coefficient, η^+, measured using the parallel-disk ($\square$), the cone-and-plate with unmodified sample ($\blacksquare$), and the cone-and-plate with donut sample ($\diamond$). Reprinted with permission from Ref. 35.

has a broadened overshoot and enhanced steady state plateau. These behaviors are even more exaggerated in the transient normal stresses.

The geometries described above all have limitations to their effective use in rheological measurements of fiber suspensions, especially in measuring the transient material functions. Ideally, any rheological measurement should be performed in a "sufficiently large" device so that the boundary and flow field effects are minimized. In the future it is expected that sliding plate rheometers, such as that developed by Giacomin et al. [36], will be more widely used; though these too suffer from finite absolute strain limitations.

Capillary rheometers are used to investigate the high shear rate rheology $\dot{\gamma} >$ 10 s^{-1}. In this case the suspension is forced through an abrupt contraction and the pressure drop is measured across the contraction and capillary length. Studies have shown that particle migration can occur away from the channel wall across streamlines, in laminar flow, due to small inertia and wall effects termed *tubular pinch* [37, 38]. The degree of particle migration in fiber suspensions is ill-defined. However, if migration does occur away from the boundaries, the regions of highest shear rates close to the capillary wall could contain a far less concentration of fibers, which results in a stress response similar to the pure matrix.

4.3 RIGID FIBERS

4.3.1 Dilute Suspensions: Fiber-Orientation Kinematics

The orientation of a single fiber can be described with a unit vector **u** along the major axis as shown in Figure 4.3, where φ and θ are the azimuthal and zenith angles, respectively. The components of **u** in spherical coordinates are
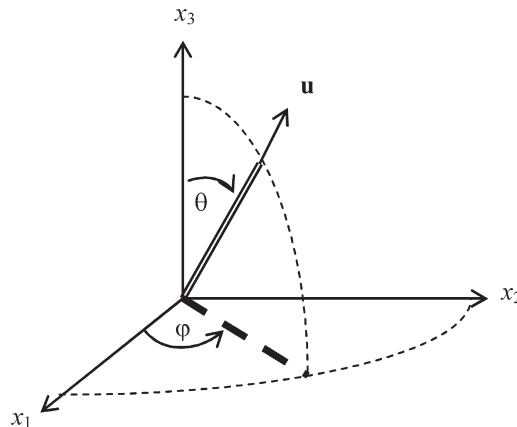
FIGURE 4.3 Unit vector **u** describing the orientation state of a fiber in spherical coordinates. Reprinted with permission from Ref. 26.

$$u_1 = \sin\theta\cos\varphi \tag{4.3}$$

$$u_2 = \sin\theta\sin\varphi \tag{4.4}$$

$$u_3 = \cos\theta \tag{4.5}$$

In the following section when discussing simple shear flow ($v_1 = \dot{\gamma}\, y$ and $v_2 = v_3 = 0$) we define x_1 as the flow direction, x_2 the direction of the velocity gradient, and x_3 the neutral or vorticity direction.

The first theoretical work that is easily extendable to rigid fibers is that of Jeffery [39]. Jeffery extended Einstein's [40] approach to solving the equations of motion for the flow of a Newtonian fluid around a spherical particle to that of a neutrally buoyant ellipsoidal particle in the absence of Brownian motion. Following Jeffery's analysis, in spherical coordinates, the rotation of an ellipsoid subject to simple shear flow is governed by the following differential equations:

$$\frac{\partial\varphi}{\partial t} = \frac{\dot{\gamma}}{a_r^2 + 1}(a_r^2\cos^2\varphi + \sin^2\varphi) \tag{4.6}$$

$$\frac{\partial\theta}{\partial t} = \lambda\frac{\dot{\gamma}}{4}\sin 2\theta\sin 2\varphi \tag{4.7}$$

where λ is a shape constant given by

$$\lambda = \left(\frac{a_r^2 - 1}{a_r^2 + 1}\right) \tag{4.8}$$

The analytical solutions to the system of differential equations (4.6) and (4.7) are

$$\tan\varphi = a_r\tan\left(\frac{\dot{\gamma}t}{a_r + a_r^{-1}} + k\right), \tan k = \left(\frac{1}{a_r\tan\varphi_0}\right) \tag{4.9}$$

$$\tan\theta = \frac{Ca_r}{\sqrt{a_r^2\sin^2\varphi + \cos^2\varphi}}, C = \frac{\tan\theta_o}{\sqrt{a_r^2\sin^2 k + \cos^2 k}} \tag{4.10}$$

where C and k are constants that may be obtained from initial orientation of the ellipsoid, φ_o and θ_o. Both $\varphi(t)$ and $\theta(t)$ are functions of time and are periodic resulting in a 3D orientation that never reaches a steady state under dynamic conditions termed a Jeffery orbit. The relative time lapse during rotation depends on the particle's initial orientation, aspect ratio, and shear rate seen by the particle. High a_r particles spend the majority of time aligned parallel to the direction of flow [6]. The period of rotation, T, required for a rotation of 2π about the particle center of mass is:

$$T = \frac{2\pi}{\dot{\gamma}} \left(a_r + \frac{1}{a_r} \right) \tag{4.11}$$

Predictions for the analytical solution to Jeffery's analysis that clearly show the periodicity of the particles orientation can be seen in Figure 4.4a. which is a graphical representation of (4.9) and (4.10) for an ellipsoidal particle with an $a_r = 5$ and initial orientation conditions $\varphi_o = 175^o$ and $\theta_o = 45^o$.
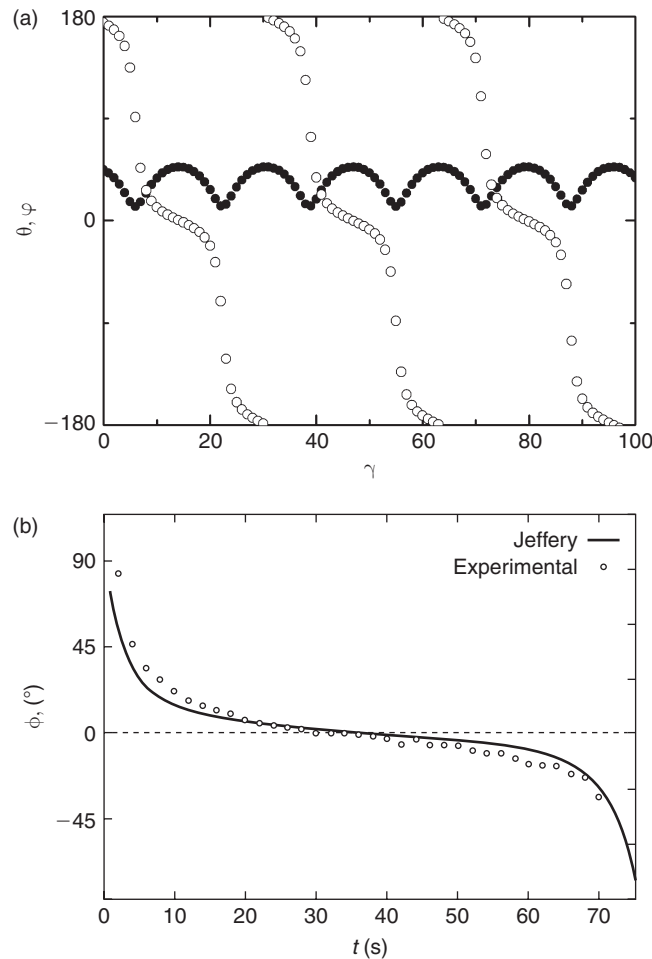
FIGURE 4.4   (a) Zenith and azimuthal angles defining the orientation of an ellipsoidal particle in simple shear flow as predicted by the analytical solution to the Jeffery's equation of motion, (5.9) and (5.10). The solution is for an ellipsoid with $a_r = 5$ with initial conditions of $\varphi_o = 175^o$, $\theta_o = 45^o$. Reprinted with permission from Ref. 41. (b) Evolution of a nylon fiber compared to predictions of Jeffery's equation. Reprinted with permission from Ref. 42.

The above analysis pertains to ellipsoidal particles but the theory can be extended to non-ellipsoidal particles by using an effective aspect ratio (a_{re}) that can be determined by comparing the rate of rotation and a_r of a particle [43]. Work has been done both theoretically [44, 45] and empirically [31, 46] to establish relations between the particle shape and a_{re}. Cox [44] found a_{re} for blunt ended bodies to be represented by

$$a_{re} = \frac{1.24a_r}{(\ln a_r)^{1/2}} \tag{4.12}$$

This work suggests that for blunt ended particles $a_{re} < a_r$ and, therefore, they have a slower period of rotation than particles with a rounded end. An exception to this trend would be for $a_r < 4.8$, in which case (4.12) predicts $a_{re} > a_r$.

Experimentally, Jeffery orbits have been observed in various systems containing high aspect ratio particles [42, 47−49]. The transient shear response of a dilute suspension of rigid fibers in a Newtonian suspending medium under simple shear flow conditions will rotate around a vorticity axis unless acted upon by another force, i.e., direct contact and/or hydrodynamic interactions between other particles or boundaries [47]. This behavior can be seen in Figure 4.4b for a single nylon fiber, $a_{re} = 27.5$, suspended in a Newtonian fluid subject to simple shear flow. Though the predictions using Jeffery's equation seem to agree well with experimental results, Moses et al. [42] state the model tends to overpredict the rate of fiber reorientation.

In the limit that $a_r \rightarrow \infty$, then $\lambda \rightarrow 1$ and the solution to (4.9) and (4.10) can be simplified, in which the equations are a function of strain, $\gamma = \dot{\gamma}t$, only:

$$\tan\theta = \tan\theta_o \sqrt{\gamma^2 \sin^2\varphi_o + 2\gamma \sin\varphi_o \cos\varphi_o + 1} \tag{4.13}$$

$$\tan\varphi = \frac{1}{\cot\varphi_o + \gamma} \tag{4.14}$$

In this case the solution is no longer periodic, or simply, the period of rotation is infinite. As a result, a particle will rotate from its initial orientation to align itself in the flow direction. This can be seen in Figure 4.5, which graphically depicts the solutions to (4.13) and (4.14) for various initial conditions. For a more in-depth discussion of the motion of a fiber predicted by Jeffery's analysis, the reader is referred to Barbosa and Bibbó [41].

Equations (4.6) and (4.7) can be generalized for any flow field in terms of **u** leading to [48−50],

$$\dot{\mathbf{u}} = \frac{D\mathbf{u}}{Dt} = \mathbf{W} \cdot \mathbf{u} + \lambda[\mathbf{D} \cdot \mathbf{u} - \mathbf{u}(\mathbf{u} \cdot \mathbf{D} \cdot \mathbf{u})] \tag{4.15}$$
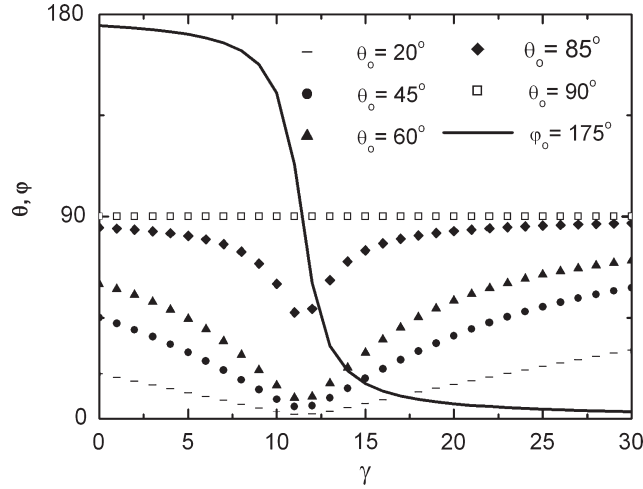
FIGURE 4.5 Evolution of orientation for an ellipsoidal particle with infinitely large a_r subject to simple shear flow as predicted by (5.13) and (5.14). Predictions were subject to the initial conditions $\varphi_o = 175°$, $\theta_o = 20°$, 45°, 60°, and 90°. Reprinted with permission from Ref. 41.

where $\dot{\mathbf{u}}$ is the substantial time derivative of the unit vector $\mathbf{u}$, $\mathbf{W} = [(\nabla v)^t - \nabla v]/2$ is the vorticity, and $\mathbf{D} = [\nabla v + (\nabla v)^t]/2$ is the rate of strain tensor and $\nabla v = \partial v_j / \partial x_i$. Because the particles are assumed rigid and inextensible, $\mathbf{u}$ $(\mathbf{u} \cdot \mathbf{D} \cdot \mathbf{u})$ is subtracted, which is the term associated with stretch along the primary axis of a flexible particle or molecule. Equation (4.15) can be simplified further, in limiting case that $\lambda \to 1$ and by noting the quantity $(\mathbf{u} \cdot \mathbf{W} \cdot \mathbf{u})$ is zero due to the antisymmetric nature of $\mathbf{W}$, as [6, 51]

$$\dot{\mathbf{u}} = \nabla \mathbf{v} \cdot \mathbf{u} - \mathbf{u}(\mathbf{u} \cdot \nabla \mathbf{v} \cdot \mathbf{u}) \tag{4.16}$$

We now consider the case of an ideal suspension, which consists of a large number of fibers that are identical in size and shape and homogeneously dispersed. To predict the motion of such a suspension using (4.15) or (4.16) one would have to track the movement of each fiber from its initial condition, resulting in an overwhelming amount of computational effort. Fortunately the fiber orientation state can be easily represented using a distribution function, $\psi(\theta, \varphi, t)$, that describes the probability of a rod at time t being in the range θ, φ to $\theta + d\theta, \varphi + d\varphi$. In certain cases, it is convenient to represent the distribution function in terms of the unit vector $\mathbf{u}$ as $\psi(\mathbf{u}, t)$. The distribution function is normalized so that the integral over the unit sphere is equal to unity:

$$\int_0^{2\pi} \int_0^{\pi} \psi(\theta, \varphi, t) \sin \theta \, d\theta \, d\varphi = \int \psi(\mathbf{u}, t) d\mathbf{u} = 1 \tag{4.17}$$

ψ (**u**, t) must also be symmetric, i.e., ψ (**u**) = ($-$**u**). This is a result of rod symmetry in that a rod whose orientation is **u** is indistinguishable from one whose orientation is $-$ **u** [5, 6]. Finally the distribution function must be able to describe the evolution of fiber orientation under dynamic conditions, termed the continuity condition [51]. To satisfy this condition one must employ a convection-diffusion type of equation. The equation used by Doi [52] and commonly referred to by others is the Smoluchowski equation or a modified Fokker-Planck equation [53]. The Smoluchowski equation is a macroscopic description of a multiparticle system. For a suspension of non-interacting fibers subject to an external flow field and neglecting Brownian motion the Smoluchowski equation can be written in the simple form:

$$\frac{D\psi}{Dt} = -\frac{\partial}{\partial u} \cdot (\dot{\mathbf{u}}\psi) \tag{4.18}$$

Equation (4.18) is valid for any $\dot{\mathbf{u}}$. For dilute suspensions we can substitute (4.16) into (4.18):

$$\frac{D\psi}{Dt} = -\frac{\partial}{\partial \mathbf{u}} \cdot [(\nabla\mathbf{v} \cdot \mathbf{u})\psi - \mathbf{u}(\mathbf{u} \cdot \nabla\mathbf{v} \cdot \mathbf{u})\psi] \tag{4.19}$$

Using the distribution function for predicting the particle orientation in complex flows is cumbersome because the amount of information computed is so large. For this reason, most theoretical work has been formulated around having to calculate the distribution function explicitly. Typically, this is accomplished with orientation tensors [5]. Using the distribution function, an infinite number of even-order tensors can be formulated that define an averaged orientational state of the system, often referred to as structure tensors. The structure tensors of interest with respect to modeling fiber suspensions are the second- and fourth-order tensors defined as:

$$\mathbf{A}(t) = \int \mathbf{uu}\psi(\mathbf{u}, t)d\mathbf{u} \tag{4.20}$$

$$\mathbf{A}_4(t) = \int \mathbf{uuuu}\psi(\mathbf{u}, t)d\mathbf{u} \tag{4.21}$$

The trace of **A** is always equal to 1 and for a completely random orientation state **A** = 1/3 **I**, where **I** is the unity tensor. In the limit that all the fibers are perfectly aligned in the x_1 direction the only nonzero component is $A_{11} = 1$. The fourth-order tensor arises in the theoretical analysis for both the particle motion and in calculating the contribution of the hydrodynamic interaction of the fibers to the extra stress. For a more complete description of orientation tensors and their use in representing fiber suspensions the reader is referred to Advani and Tucker [5].

To obtain an evolution equation in a form containing $\mathbf{A}$, when the distribution function is unknown, one must take the material derivative of (4.20) and substitute in the governing equation for ψ and $\dot{\mathbf{u}}$, (4.18), on the right-hand side. Integration by parts, with some simplification, leads to

$$\frac{D\mathbf{A}}{Dt} = \mathbf{A} \cdot \nabla \mathbf{v} + \lambda[(\mathbf{A} \cdot \nabla \mathbf{v})^t - 2\mathbf{D} : \mathbf{A}_4] \qquad (4.22)$$

To solve this equation a closure approximation is need to express $\mathbf{A}_4$ in terms of $\mathbf{A}$. Equation (4.22) is also commonly written in the following form [5]

$$\frac{D\mathbf{A}}{Dt} = (\mathbf{W} \cdot \mathbf{A} - \mathbf{A} \cdot \mathbf{W}) + \lambda(\mathbf{D} \cdot \mathbf{A} + \mathbf{A} \cdot \mathbf{D} - 2\mathbf{D} : \mathbf{A}_4) \qquad (4.23)$$

The fourth-order tensor $\mathbf{A}_4$ has been the subject of much research because to complete the analysis one must use a closure or decoupling approximation to express the fourth-order tensor in terms of the second-order tensor. A closure approximation is some function that approximates a higher-order orientation tensor with lower-order orientation tensors and/or the invariants of lower-order orientation tensors. In the context of this chapter the closure approximation is vital in establishing an equation of change for the average orientation state of the system and in calculating the extra stress contribution as a result of the hydrodynamic drag discussed later. In addition the higher-order orientation tensors (tensors greater than second-order) arise in any continuum model that describes the mechanical or rheological properties of a two-phase system containing particles whose orientation can be anisotropic. Numerous closure approximations have been suggested and tested, which are beyond the scope of this text. The reader is directed to the works of Hand [54], Hinch and Leal [55], Barthés-Biesel and Acrivos [56], Advani an Tucker [57], Chung and Kwon [58], and Jack and Smith [59] for in-depth reviews.

4.3.2 Dilute Suspensions: Rheology

4.3.2.1 Theory A general expression for the total stress in a dilute suspension of high aspect ratio non-Brownian particles can be derived from the theories of Hand [54] and Giesekus [48] and is commonly referred to as the Lipscomb model [60, 61]

$$\sigma = -P\mathbf{I} + 2\eta_s\mathbf{D} + 2c_1\phi\eta_s\mathbf{D} + 2\phi\eta_s N\mathbf{D} : \mathbf{A}_4 \qquad (4.24)$$

where $\boldsymbol{\sigma}$ is the total stress, η_s is the suspending medium viscosity, c_1 is a constant, and N is a dimensionless parameter that represents the coupling between hydrodynamic stress contribution and the fiber orientation. The third term on the right side of the equation is the viscosity enhancement as a result of the fiber

and is similar to the enhancement term for a dilute suspension of spheres proposed by Einstein [40]. Lipscomb et al. [60] gives c_1 to be equal to 2. The fourth term on the right side of the equation is the contribution to stress from the hydrodynamic drag of the fluid over the fiber. As in the equation for evolution of fiber orientation, a closure approximation is needed in (4.24) to express $\mathbf{A_4}$ in terms of $\mathbf{A}$. Using (4.24) it is straightforward to show that the shear stress growth coefficient, η^+, and the first normal stress growth function, $N_1{}^+$, are

$$\eta^+ = \sigma_{12}/\dot{\gamma} = \eta_s[1 + \phi(c_1 + 2NA_{1212})] \tag{4.25}$$

$$N_1^+ = 2\phi\eta_s\dot{\gamma}N(A_{1112} - A_{2212}) \tag{4.26}$$

where the fourth-order tensor components are a function of time and can be predicted with the analysis presented in Section 4.3.1. pertaining to the evolution of fiber orientation.

For dilute suspensions Lipscomb et al. [60] gives N to be a function of fiber aspect ratio,

$$N = \frac{a_r^2}{2\ln a_r} \tag{4.27}$$

Other works for dilute suspensions such as Batchelor [11] give N to be a function of the number of fibers per unit volume, c, and/or fiber length, L, and aspect ratio.

$$N = \frac{a_r^2}{3\ln(2a_r)}f(\varepsilon),\ f(\varepsilon) = \frac{1 + 0.64\varepsilon}{1 - 1.5\varepsilon} + 1.659\varepsilon^2,\ \varepsilon = [\ln(2a_r)]^{-1} \tag{4.28}$$

4.3.2.2 *Experimental Characterization*

4.3.2.2.1 Viscosity It is clear from fiber suspension theory that the bulk extra stress of a fiber suspension subject to shear flow is intimately linked to the fiber orientation. In the case of dilute suspensions where fibers will continue to rotate around the vorticity axis an oscillating stress response that is a function of the orientation state of the particle has been experimentally observed. Figure 4.6 depicts the oscillating shear stress upon startup for a dilute suspension of fibers in a Newtonian fluid by way of the specific viscosity normalized by the fiber concentration η_{sp}/ϕ, vs. time, normalized by the period of fiber rotation. The decay of the stress oscillation is believed to be a result of several interaction, including boundary, particle–particle, hydrodynamic or slight aspect ratio variations [63]. In most reported rheological measurements of dilute suspensions stress oscillations decay to a steady state, which exhibits an enhanced
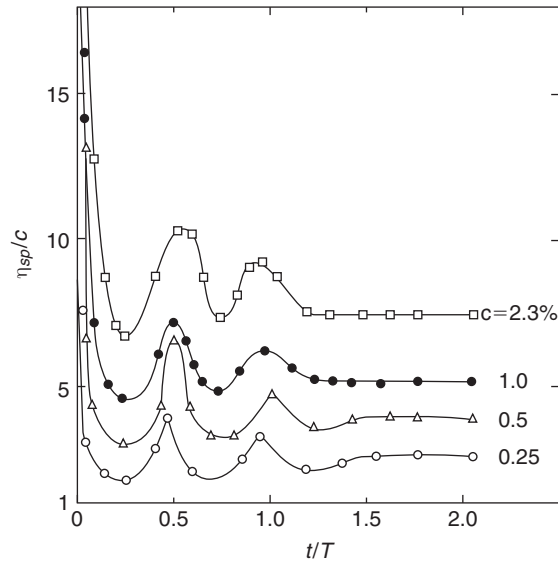
FIGURE 4.6   Start-up of shear flow experiment depicted through the specific viscosity ($\eta_{sp} = \eta_r - 1$), normalized by the glass fiber volume fraction, vs. time, normalized by the period of oscillation T. Tests were performed with a dilute suspension of rigid rods of varying concentration and constant aspect ratio, $a_r = 5.2$, in a Newtonian suspending medium. The rods were initially aligned parallel to the direction of velocity gradient with the use of an electric field. All tests were performed on a torsional cone-and-plate rheometer at $\dot{\gamma} = 2.51$ s^{-1}. Reprinted with permission from Ref. 62.

viscosity compared to the suspending medium and follows similar trends to the theory.

Shear thinning behavior of dilute fiber suspensions in Newtonian fluids has been observed. Ganani and Powell [64] who reviewed much of the early literature found that for suspensions containing fibers with aspect ratios in the range of 35−45, a weak shear thinning behavior was noticed at low shear rates followed by a Newtonian plateau $\dot{\gamma} > 10$ s^{-1}. For fibers with $a_r > 100$, the authors found a strong shear rate dependence over a broad shear rate range of 0.1−100 s^{-1}. When considering the theory, (4.25), the source of this non-linear behavior becomes more evident as the only parameter with a shear rate dependence is the fiber orientation. Polydispersity, initial orientation, inhomogeneities in the system, and hydrodynamics can all play an important role resulting in a distribution of orientation states that can vary with shear rate.

The literature pertaining to dilute suspensions in non-Newtonian fluids is limited because in most cases the stresses are dominated by the suspending medium and difficult to measure. However, what is available suggests the viscosity increase is proportional to the fiber concentration. In highly viscoelastic fluids stress oscillations are rare and if present will dampen after one

oscillation period. This is a result of competing viscoelastic and hydrodynamic effects [65, 66].

4.3.2.2.2 Normal Stress   Dilute fiber suspensions in Newtonian suspending media can exhibit a nonzero first normal stress function, N_1, which displays a similar connection to the fiber orientation as the shear stress. An oscillating fiber orientation will manifest in the form of a transient and oscillating N_1^+. If steady state in the fiber orientation is reached, N_1 has been found to be linearly proportional to the shear rate and suspending medium viscosity. These trends have been shown experimentally and coincide with theory, as in (4.26). Nonzero normal stresses in fiber suspensions with Newtonian suspending media arise when the fiber orientation has a component out of the plane of shear and is not a result of enhanced elasticity. This becomes more apparent when considering dilute suspensions in non-Newtonian suspending media. A small amount of fiber or dilute suspensions can display a decrease in N_1 compared to the neat fluid before rising in proportionality to ϕ [67].

4.3.2.2.3 Small-Amplitude Oscillatory   In small-amplitude oscillatory measurements of dilute fiber suspensions in Newtonian suspending media only the real or viscous component of the complex viscosity and complex modulus exist [68]. This reaffirms that rigid fibers do not contribute to elasticity. In contrast, the normal stresses that can arise are directly related to the fiber orientation component out of the shear plane. Small-amplitude oscillatory measurements will be discussed in more detail in the section pertaining to nondilute suspensions.

4.3.3 Nondilute Suspensions: Fiber-Orientation Kinematics

4.3.3.1 Semidilute Suspensions   In semidilute suspensions the oscillations present in the dilute suspensions are less common. This is a direct result of the contributing factors that can dampen the oscillations being more prevalent as the fiber concentration is increased. The common approach to predict this behavior relies on Jeffery's equation for the fiber orientation with the assumption that the fiber is infinitely long [11], or $\lambda = 1$, in which case,

$$\frac{D\mathbf{A}}{Dt} = (\mathbf{W} \cdot \mathbf{A} - \mathbf{A} \cdot \mathbf{W}) + (\mathbf{D} \cdot \mathbf{A} + \mathbf{A} \cdot \mathbf{D} - 2\mathbf{D} : \mathbf{A}_4) \tag{4.29}$$

As discussed in Section 4.3.1, the predictions are no longer periodic but transient in that the fibers will rotate from their initial orientation state to align in the flow direction.

4.3.3.2 Concentrated Suspensions   In the first attempts at simulating the fiber orientation of concentrated suspensions in mold filling, Jeffery's equation for infinitely long fibers, (4.29), was used [69]. Comparison between fiber orientation measurements of injection-molded parts and simulation results

suggested Jeffery's equation overpredicts the degree of alignment and the shear strain needed to align the fibers. As a result Folgar and Tucker [70] modified Jeffery's theory to include a phenomenological term that prevents full alignment of fiber orientation, termed the Folgar-Tucker (F-T) model. The F-T model can be written in terms of $\mathbf{A}$ as follows [5]

$$\frac{D\mathbf{A}}{Dt} = (\mathbf{W} \cdot \mathbf{A} - \mathbf{A} \cdot \mathbf{W}) + (\mathbf{D} \cdot \mathbf{A} + \mathbf{A} \cdot \mathbf{D} - 2\mathbf{D} : \mathbf{A_4}) + 2C_I \dot{\gamma}(\mathbf{I} - 3\mathbf{A}) \qquad (4.30)$$

where C_I is a phenomenological parameter. The last term on the right-hand side of the equation is similar to the isotropic diffusivity term in theories for Brownian rods [9]. The F-T model allows for the control of the steady-state fiber orientation through the magnitude of C_I, but the rate of fiber reorientation is dominated by the flow field for the case of small C_I, which is typically in the range of $0.016-0.0001$ [71]. Currently, there is no theoretical approach for calculating the interaction coefficient, C_I, in the F-T model and is determined by fitting predictions to experimental results, which can be time intensive to produce [72]. Bay [71] developed an empirical expression for concentrated suspensions that is a function of the fiber volume fraction and aspect ratio as

$$C_I = 0.0184 \exp(-0.7148\phi a_r) \qquad (4.31)$$

Equation (4.31) predicts that C_I decreases for increasing ϕa_r and represents fiber screening. Phan-Thien et al. [73] proposed a model in which C_I increases with increasing ϕa_r as

$$C_I = m_1[1.0 - \exp(-m_2\phi a_r)] \qquad (4.32)$$

where m_1 and m_2 are fit parameters, which they found to be, $m_1 = 0.03$, $m_2 = 0.224$.

The F-T model improves the predictions of the steady-state fiber orientation but has little effect on the strain at which the steady-state orientation occurs. In an attempt to control the rate of fiber reorientation, Huynh [74] and Sepehr et al. [75] both included a term to reduce the rate of fiber orientation termed the strain reduction factor by Huynh and the slip coefficient by Sepehr. The slip coefficient, α, can be added to the F-T model as follows

$$\frac{D\mathbf{A}}{Dt} = \alpha[(\mathbf{W} \cdot \mathbf{A} - \mathbf{A} \cdot \mathbf{W}) + (\mathbf{D} \cdot \mathbf{A} + \mathbf{A} \cdot \mathbf{D} - 2\mathbf{D} : \mathbf{A_4}) + 2C_I \dot{\gamma}(\mathbf{I} - 3\mathbf{A})] \qquad (4.33)$$

and has a value between 0 and 1. However, the addition of the slip or strain reduction factor to the equations governing fiber motion results in a loss of objectivity of the equation. This becomes important when the coordinate frame is translated or rotated as might be required in complex flow simulations of mold filling. However, the physical aspects of the predictions, in the case of simple shear flow, are still acceptable.

Model predictions of fiber orientation using the strain reduction factor in combination with the F-T model show an improved agreement with experimental fiber orientation in simple flow and complex flows in injection molded plaques. Figure 4.7 depicts the experimental fiber orientation in startup of simple shear flow with predictions of the fiber orientation using the F-T model with slip and two values of C_I. The value $C_I = 0.006$ was determined by fitting and $C_I = 0.0001$ represents small C_I. Predictions of the F-T model with the slip parameter seem to agree with the limited experimental data. However, there is evidence that suggests that the fiber component in the 2-direction increases at small strains to unpredicted values, which is attributed to fiber contact [25].

Wang et al. [76] suggested a model in which the rate of fiber orientation could be reduced without violating objectivity as

$$
\frac{D\mathbf{A}}{Dt} = (\mathbf{W} \cdot \mathbf{A} - \mathbf{A} \cdot \mathbf{W}) + \{\mathbf{D} \cdot \mathbf{A} + \mathbf{A} \cdot \mathbf{D} - 2[\mathbf{A}_4 + \\
\dots (1 - \alpha)(\mathbf{L}_4 - M_4 : \mathbf{A}_4)] : \mathbf{D}\} + 2\alpha C_I \dot{\gamma}(\mathbf{I} - 3\mathbf{A}) \tag{4.34}
$$

where $\mathbf{L}_4$ and $\mathbf{M}_4$ are functions of $\mathbf{A}$. Equation (4.34) is nearly identical to the F-T model with the slip parameter. The difference is $\mathbf{A_4}$ is replaced by a reduced-strain
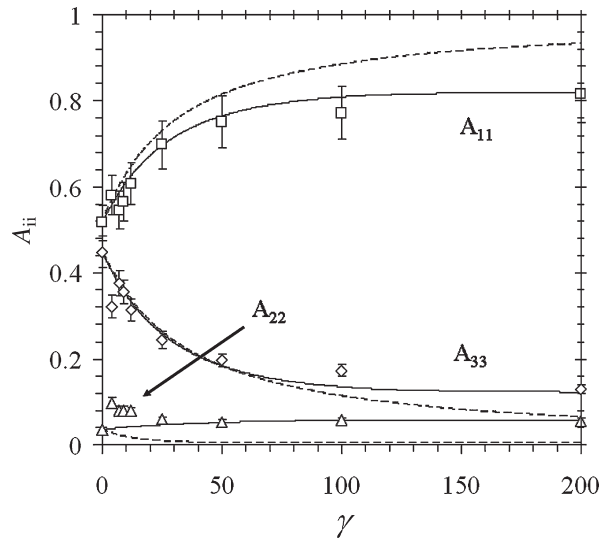
FIGURE 4.7 Experimental and predicted fiber orientation represented through the A_{ii} components in startup of simple shear flow at $\dot{\gamma} = 1$ s^{-1}. The data points are for a concentrated short fiber suspension ($\phi = 0.1766$, $a_r = 28.2$) with a polybutylene terephthalate matrix. The lines represent the predictions of the Folgar-Tucker model with the addition of a slip term with $\alpha = 0.3$, $C_I = 0.0001$ (dashed line) and $C_I = 0.006$ (solid line). Reprinted with permission from Ref. 26.

closure approximation $[\mathbf{A}_4 + (1-\alpha)(\mathbf{L}_4 - \mathbf{M}_4 : \mathbf{A}_4)]$ and is the origin of the term *Reduced-Strain Closure* (RSC) model. The model gives similar predictions to the F-T model with slip while maintaining material objectivity. Note (4.34) still contains $\mathbf{A}_4$ which can be expressed in terms of $\mathbf{A}$ with any available closure.

4.3.4 Nondilute Suspensions: Rheology

4.3.4.1 Semidilute Suspensions In the semidilute regime interparticle hydrodynamic interaction is the predominant phenomenon that can affect the dynamic behavior of the fiber microstructure and contribute to the extra stress. The functional form of the extra stress in this regime is the same as that in the dilute case, (4.24). However, N is more complex and accounts for interparticle hydrodynamics. Dinh and Armstrong [51] followed the slender body theory of Batchelor to estimate the hydrodynamic drag as a function of interparticle spacing as,

$$N = \frac{a_r^2}{3\ln(2h/D)} \quad h = \begin{cases} \left(nL^2\right)^{-1} & \text{random} \\ \left(nL\right)^{-\frac{1}{2}} & \text{aligned} \end{cases} \tag{4.35}$$

where h is the interparticle spacing given for a completely random and aligned fiber orientation, and D is the fiber diameter. As with some semidilute theories, Dinh and Armstrong set c_1 equal to zero in (4.24).

Predictions for the Dinh and Armstrong model are well documented and will be reviewed here: first in the case of simple shear flow, then elongational flow. In startup of shear flow, the viscosity of the suspension is greater than the solvent viscosity by a factor of nL^3 and the normal stress difference coefficients are equal to zero. The transient shear viscosity and normal stress difference coefficients are a function of shear strain alone and not shear rate. At large strains η^+ approaches the viscosity of the suspending medium, $\eta^+ \lim_{\gamma \to \infty} \to \eta_s$.

This is a direct result of the approximation of the hydrodynamic drag on the fiber by a line integral along the backbone of the fiber. The thickness is neglected in the calculation, resulting in no contribution to the extra stress, which becomes apparent when the fibers fully align in the principle flow direction. The transient first normal stress differences approach zero at large strains. The dimensionless elongational stress growth viscosity is a function the Hencky strain alone and not the strain rate [54, 77, 78].

Shaqfeh and Fredrickson [79] proposed a theory for dilute and semidilute suspensions that was based on a diagrammatic representation of the multiscattering expansion for the averaged Green's function to obtain an expression for the hydrodynamic energy dissipation from viscous drag of the fluid on the particle. For an isotropic fiber orientation distribution they give

$$N = \frac{4a_r^2}{3} \left\{ \frac{1}{\ln(1/\phi) + \ln\ln(1/\phi) + C} \right\} \tag{4.36}$$

where C'' is a constant given as $C'' = -0.66$, and 0.16 for random and aligned, respectively. Phan-Thien and Graham [80] proposed the following phenomenological expression

$$N = \frac{a_r^2(2-\phi/G_v)}{2[\ln(2a_r)-1.5](1-\phi/G_v)^2} \tag{4.37}$$

where $G_v = 0.53 - 0.013a_r$, for the range of $5 < a_r < 30$. The predictions of both the theories of Shaqfeh and Fredrickson and Phan-Thien and Graham are similar to that of the Dinh and Armstrong [51] model with the exception of the magnitude of the transients which are linked to the value of N.

4.3.4.2 *Concentrated Suspensions*   Currently there is no theory for concentrated suspensions that accounts for fiber contact. However, semidilute theory has been used to some extent to model their stress behavior, in which case N is fit to the rheological material functions of a fluid instead of calculating N from theory [71, 81, 82].

4.3.4.3 *Viscoelastic Matrices*   In the majority of fiber composites of industrial significance the matrix is polymeric and exhibits nontrivial viscoelastic behavior, which increases the complexity of modeling such suspensions. The first attempts ignore the fiber and treat the suspension as a homogeneous viscoelastic fluid [81]. Advances in the field have emphasized the importance of including the fibers to the stress formalism and current treatment includes the fiber and suspending medium by viewing the system as a bicomponent fluid [77, 78, 83].

4.3.5   Nondilute Suspensions: Experimental Characterization

4.3.5.1 *Steady-State Shear Rheology*   In addition to an enhanced viscosity, nondilute fiber suspensions in Newtonian suspending media commonly exhibit a pronounced shear thinning response. The degree of shear thinning can be a function of fiber concentration, length, and suspending medium viscosity. This behavior is attributed to the destruction of transient network structures of fibers at increasing shear rates [2].
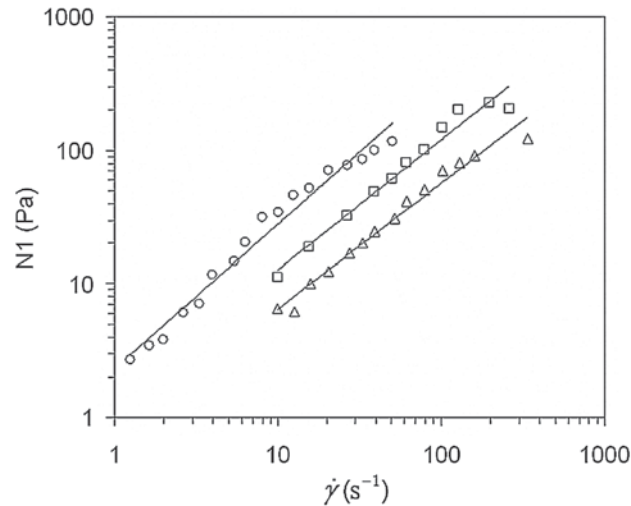
Suspensions with non-Newtonian suspending media can exhibit various shear thinning behaviors. Multiple factors can contribute to the shear thinning, the most dominant of which being the fiber network, and the suspending medium shear thinning characteristics. In general, the shear viscosity of

suspensions containing low concentrations of low aspect ratio fibers (in the dilute and semidilute regime) usually approach a Newtonian plateau at low shear rates, and in many instances show little change from the behavior of the neat matrix [34]. The shear viscosity of suspensions containing a high concentration of fibers or fibers with a large aspect ratio (in the concentrated regime), exhibits a more pronounced behavior. At low shear rates the shear viscosity can exhibit a Newtonian plateau or rise in an unbounded manner and exhibit yield-like characteristics [84]. At high shear rates, shear thinning can occur at a reduced shear rate, which can result in a shear viscosity similar to that of the neat suspending medium. However, not all concentrated samples display yield-like behavior. Guo et al. [85] reported the absence of yield-like behavior for a high volume fraction $\phi = 0.384$ suspension in low-density polyethylene. The source of yielding is most likely complex interactions between the suspending medium and the fiber surface, which may not be present in all suspensions.

The more pronounced effect of fibers on shear viscosity at low shear rates and decreased effects at high shear rates is a reflection of changes in the suspension's microstructure [34]. For non-Brownian fiber suspensions the fiber orientation distribution is irreversibly changed by flow and leads to a shear history dependent rheology [34]. Higher shear rates impart a higher degree of fiber orientation in the flow direction [84]. As a result, a sample that is presheared may not exhibit the same shear viscosity compared to a sample that has not been sheared or has an isotropic fiber orientation distribution [86].

It is well established that nondilute fiber suspensions in Newtonian suspending media will exhibit a steady state N_1. This can be seen in Figure 4.8, which depicts the N_1 dependence on suspending medium viscosity at similar fiber concentration and a_r. Experimentally, the magnitude of N_1 follows a linear trend with shear rate, suspending medium viscosity, and fiber concentration, which coincides with theory [2]. Delineating the source of N_1 in non-Newtonian suspending media is not straightforward. The contribution to N_1 from the elasticity in the suspending medium is suppressed by the fiber [2]. However, it is speculated that the contribution from the fiber is consistent with theory. The mechanisms that contribute to the suppression of the elasticity are poorly understood but manifest in important processing applications such as die swell suppression.

4.3.5.2 Small-Amplitude Oscillatory Rheology The addition of fibers to a non-Newtonian fluid increases the magnitude of the complex viscosity, $|\eta^*|$; the degree of this increase depends on the concentration, aspect ratio and orientation distribution of the fibers [85, 87]. The dependence of $|\eta^*|$ on glass fiber concentration and aspect ratio is not obvious. Similar to the shear viscosity behavior at low shear rates, $|\eta^*|$ can exhibit an enhanced Newtonian plateau [85, 87] or rise in an unbound manner at low frequencies [88−90]. At high frequencies, $|\eta^*|$ can begin to merge onto that of the matrix [89] or follow a similar shear thinning curve of the matrix at a constant enhance value [85, 87]. Furthermore, $|\eta^*|$ increasingly deviates from the shear viscosity at increasing

FIGURE 4.8 N_1 vs. shear rate for various glass fiber suspensions with a constant fiber concentration ($\phi = 0.044$, $a_r = 276$) and different Newtonian suspending medium viscosities ($\triangle$, 14; $\square$, 16; $\circ$; 120 Pa·s). All measurements were performed on a torsional rheometer with cone-and-plate geometry. Reprinted with permission from Ref. 2.

fiber concentrations for both Newtonian and non-Newtonian fiber suspensions [91−94]. This suggests that the Cox-Merz relationship [95] does not hold for fiber-filled systems.

It has been speculated that small-amplitude oscillatory shear in the linear strain region is too weak to induce fiber reorientation of the same magnitude as in steady shear flow [85]. This explains why there is a discrepancy between dynamic oscillatory and steady shear rheological measurements. However, there is experimental evidence that suggests that oscillatory flow can lead to irreversible orientation changes to some degree. Kim and Song [90] reported that for a suspension containing short glass fiber-filled ($\phi = 0.1766$, $a_r \sim 21.4$, concentrated regime) in a polybutylene terephthalate matrix exhibiting weak shear rate dependence, $|\eta^*|$ changed after repeated dynamic oscillatory tests on the same sample. The repeated tests are denoted as run 1−6 in Figure 4.9a. A newly loaded sample exhibited a yield-like behavior at low frequencies. After repeated tests on the same sample a Newtonian plateau developed, suggesting irreversible fiber reorientation.

Similar to the shear viscosity, the initial orientation of the sample can have an effect on $|\eta^*|$. A sample whose initial orientation is random will exhibit a larger $|\eta^*|$ than a sample whose fiber is oriented in the flow direction. Mobuchon et al. [87] reported a reduction of over 50% in $|\eta^*|$ after preshearing a concentrated short glass fiber-filled polypropylene ($\phi = 0.124$, $a_r \sim 21.4$, concentrated regime) (Fig. 4.9b). The reduction in $|\eta^*|$ was attributed to the alignment of the fibers in the flow direction during preshearing; the greater the preshear stress the greater the overall fiber alignment.
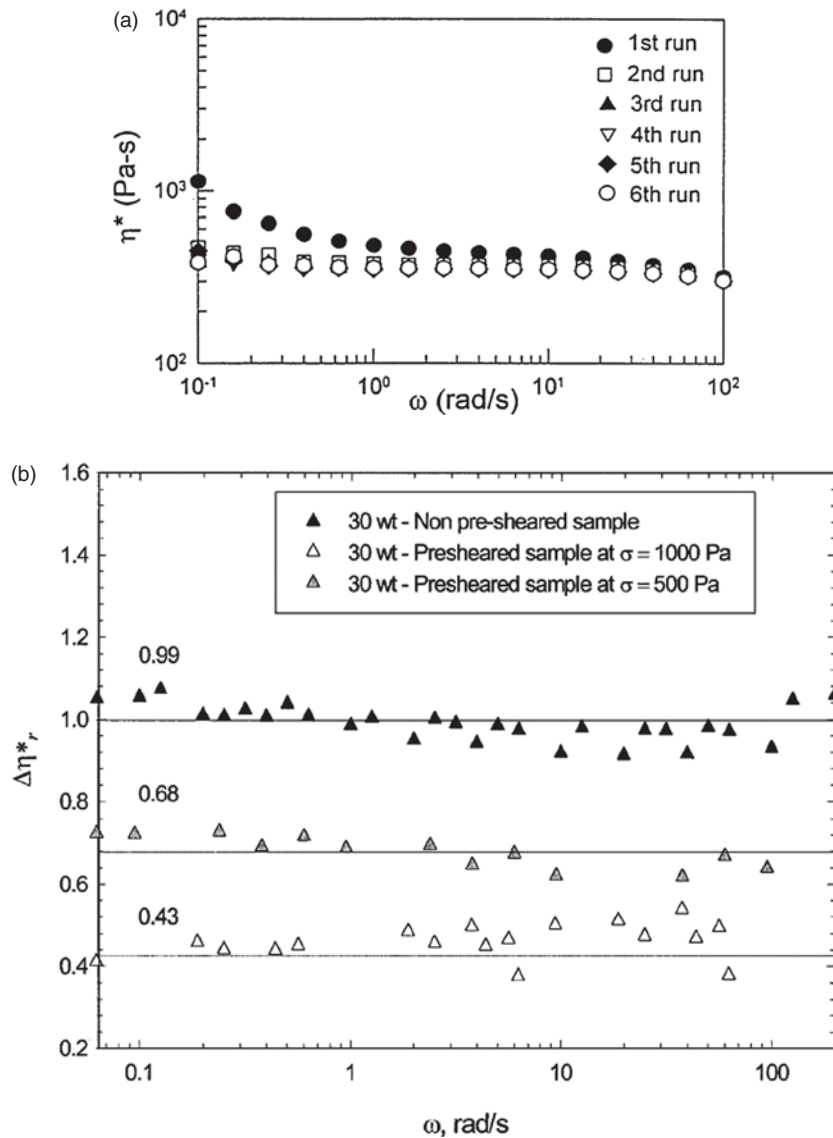
FIGURE 4.9   (a) $|\eta^*|$ in small-amplitude ($\gamma_o = 0.15$) oscillatory shear for a short glass fiber-filled polybutylene terephthalate ($\phi = 0.1766$, $a_\mathrm{r} \sim 21.4$, concentrated regime). Reprinted with permission from Ref. 90. (b) The effects of preshear on $|\Delta\eta_r^*|$ vs. frequency for a short glass fiber-filled polypropylene ($\phi = 0.124$, $a_\mathrm{r} \sim 21.4$, concentrated regime). In this case $|\Delta\eta_r^*|$ is the magnitude of the complex viscosity of the presheared sample normalized by the no preshear sample values. Reprinted with permission from Ref. 82.

The dynamic functions of glass fiber suspensions in non-Newtonian fluids show a strain amplitude dependence that markedly increases with concentration and aspect ratio. Mutel and Kamal [96] tested PP containing short glass fibers at concentrations ranging from $10-40$ wt % ($\phi = 0.0354 - 0.1805$). They found that the addition of short glass fibers to a PP caused increasing strain amplitude dependence on increasing concentration. On the contrary, the neat PP suspending medium exhibited linear strain dependence through a range of $5-50$ strain %. Kim and Song [90] found that in a short glass fiber suspension, $|\eta^*|$ decreased at constant frequency as the strain amplitude was increased. This was attributed to larger strains increasing the average orientation of the fibers along the flow direction.

4.3.5.3 Transient Responses Nondilute fiber suspensions can exhibit profound transient rheological material functions compared to their neat suspending media. In general, the behavior is characterized by a large and irreversible overshoot in both the shear stress growth σ^+, and the first normal stress growth N_1^+, functions. It has been well established through theory and experiment that the transient features are directly connected to the presence of fibers and their orientation within the suspension. For this reason, there has recently been a drive to establish unique material parameters for fiber suspension theory by fitting to the startup of flow and flow-reversal measurements [71, 82]. Subsequently, we review the key aspects of the transient rheology in relation to the fiber orientation. Certainly, this overview is incomplete and the reader is referred to additional sources [1, 71, 97, 98].

As discussed at the beginning of the chapter, the rheology, and especially the transient rheology of fiber suspensions can be highly dependent on the rheometer geometry used to characterize suspensions in steady shear. Measurements performed using parallel disks, which impose an inhomogeneous velocity gradient field from the center of the plate to the outer rim, lead to exaggerated transients in both σ^+ and N_1^+ [35]. In these instances the overshoot peak in N_1^+ can be orders of magnitude greater than the steady-state value and take over 150 strain units to reach a steady state. However, this transient response does not represent the true stress growth material function as a suspension would exhibit in a homogenous flow field [35].

The transient stresses of nondilute fiber suspensions in both Newtonian and non-Newtonian suspending media do not show an oscillatory response, as in dilute suspensions, but rise to a peak that decays to a steady state (stress overshoot) or simply decays to a steady state value with no apparent peak. Increasing fiber concentration and/or fiber aspect ratio increases the magnitude of the overshoot and the time needed to reach steady-state in a similar manner [84]. In general, σ^+ and N_1^+ approach a steady state in roughly 50 strain units. The overshoot is a result of an evolving microstructure, where, upon flow the fibers orient themselves toward the flow direction, a phenomenon that is irreversible. This behavior is seen in Figure 4.10a, which shows a stress growth measurement of a concentrated short glass fiber filled polybutylene
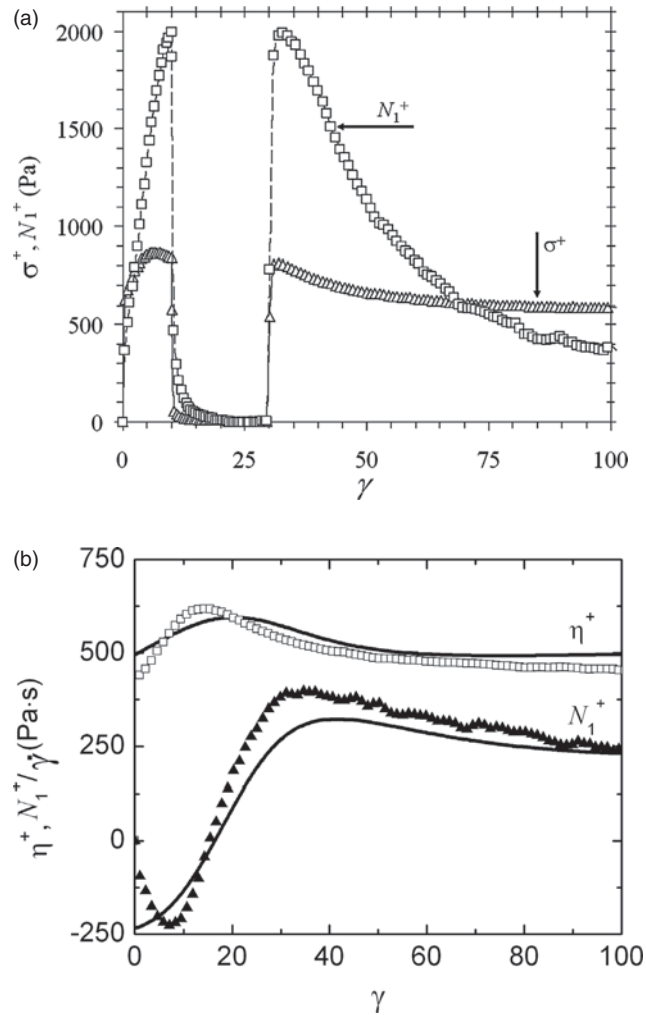
FIGURE 4.10   Shear stress growth and first normal stress growth coefficients for (a) interrupted stress growth. Reprinted with permission from Ref. 67. (b) Flow reversal following steady shear of a short glass fiber-filled polybutylene terephthalate (30 wt %). The lines represent the fit of the Folgar-Tucker model with the addition of the slip term, combined with the Lipscomb stress equation. Reprinted with permission from Ref. 67.

terephthalate (PBT), which was interrupted at the peak of the N_1^+ overshoot. When the flow was interrupted the stresses decayed to zero following the relaxation time of the neat polymer, which is consistently observed in Newtonian and non-Newtonian suspending media [99]. However, when the flow was reapplied, the stresses immediately grew to their previous value, the overshoot peak, which in turn continued to decay toward a steady state. This behavior is consistent for both σ^+ and N_1^+.

A sample whose initial fiber orientation is aligned parallel to the direction of the velocity gradient will exhibit the greatest overshoot. In contrast, a sample whose initial fiber orientation is parallel to the flow direction will exhibit the lowest overshoot, with a randomly oriented sample falling between these two ideal cases [84]. Ramazani et al. [77] showed that preshearing a sample before the stress growth experiments removed the initial overshoot exhibited by randomly oriented fiber suspensions. The peak of the shear stress overshoot scales with strain at varying shear rates and typically occurs between 2 and 10 strain units. Current theory suggests that the peak in the shear stress overshoot corresponds to an average fiber orientation of 45° with respect to the flow direction [77, 84]. Experiments that connect the fiber microstructure to the rheological measurements have shown that the shear stress growth overshoot coincides with an overshoot in the A_{12}-component. Steady state occurs when the fiber orientation reaches a steady state, generally aligned in the flow direction, although complete alignment can be restricted due to fiber interaction [72].

Flow reversal experiments provide an avenue to condition a fiber suspension sample before testing. A flow reversal test begins with a sample being sheared in one direction for a predetermined time or strain. Subsequently, the flow is applied in the opposite direction either immediately or after some period of wait time. This effectively conditions the sample, which is shear history dependent, and increases the reproducibility of the measurements. Furthermore, it leads to rather unique values of σ^+ and N_1^+. The stress response to a flow reversal experiment can be seen in Figure 4.10b by way of the shear stress growth coefficient η^+ and N_1^+ for a short glass fiber-filled PBT. Upon flow reversal η^+ exhibits an overshoot, the peak of which occurs at an increased strain compared to the overshoot of a fresh sample. More interesting is the behavior of N_1^+, which displays an initial undershoot before rising to a small overshoot that decays toward a steady state. In flow reversal, the transients are believed to be a result of the fibers, which are not completely aligned in the flow direction, tumbling backward. It is interesting that current theory is able to predict the major features of this experiment, which can also be seen in Figure 4.10a. The solid lines represent the F-T model with the addition of the slip term (4.33) combined with the Lipscomb stress equation (4.24) [67]. It has also been shown that fitting the material parameters to the transient rheology allows for the qualitative prediction of the major features in the evolution of fiber orientation when the fiber orientation is quantitatively known at some point; i.e., initial condition or steady state [26, 67]. In the future fitting could potentially be used to determine unambiguous material parameters for a given fluid that could then be used in complex flow simulations to predict fiber orientation such as in injection molding.

4.3.5.4 Extensional Viscosity   The extensional behavior of fiber suspensions as determined experimentally remains elusive and rather poorly characterized. This is a direct consequence of the difficulty in measuring this material function. Tensile elongation samples tend to elongate in a nonuniform manner

or "neck" which results in sample failure. Available data suggest the presence of fibers in a non-Newtonian fluid can lead to extensional thinning [100]. It is speculated that the thinning behavior is a result of a locally induced shear flow between the fibers. However, it is difficult to delineate material functions from the flow kinematics. Still, researchers have reported dramatic large extensional viscosities on the order of 20 to 40 times the shear viscosity [87, 101]. Research in this field would benefit from measurements performed using a lubricated squeeze flow apparatus.

4.4   FLEXIBLE FIBERS

A distinct class of fiber filled composites is one constructed from long fibers. The term *long fiber* is being used in this context to describe fibers that are able to bend or flex during processing and thus may affect both the flow behavior and material properties. The flexibility of a fiber can be easily characterized using (4.1). Because of the physical length of the long fibers, complications in measuring their rheology may exist. In this section, we discuss theory and experimental efforts of relating long fiber rheology.

4.4.1   Dilute Suspensions

4.4.1.1   Semiflexible Fiber Kinematics   The relatively limited published literature relating to flexible fibers is an indication of the difficulty associated with modeling such systems. One approach for semiflexible fibers, proposed by Strautins and Latz [102], is an extension of Jeffery's equation for rigid fibers. In this case the evolution equations are solved for two rigid rods (each rod of length l_B) connected by a joint. The joint and spring allows the two rigid rods to bend and exhibit flexibility as shown in Figure 4.11. In Figure 4.11, **p** and **q** are unit vectors associated with each of the rods of the flexible fiber. This is analogous to the unit vector **u** defined for rigid fiber theory, see, for example, Figure 4.3. However, for the case of a bead-rod fiber, there exists two rigid rods, each with an orientation dictated by either **p** or **q**. The spring allows for flexibility and resistance to bending (spring stiffness coefficient k). The beads, on the other hand, provide surface area for hydrodynamic drag. This model is used
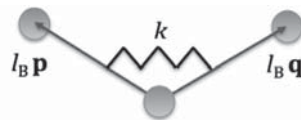
FIGURE 4.11   The Bead-Rod model consists of two rigid rods connected to a pivoting bead.

in the formulation of a continuum model that describes the motion of fibers that can bend about its center of mass. In the treatment provided by Strautins and Latz, the fiber bending is limited to small angles, hence the theory is applicable for semiflexible systems. The theory consists of two orientation tensors and one orientation vector. One orientation tensor, similar to what exists in rigid-rod theory, describes the second moment of any one of the rods with respect to the orientation distribution function and is defined in (4.39). The other orientation tensor describes the mixed product of both rigid-rod vectors with the orientation distribution function (4.40). Last, the orientation vector is defined as the first moment of the distribution function, using either orientation vector, defined in (4.41).

$$\mathbf{A} = \iint \mathbf{pp}\psi(\mathbf{p}, \mathbf{q}, t) d\mathbf{p} d\mathbf{q} \tag{4.38}$$

$$\mathbf{B} = \iint \mathbf{pq}\psi(\mathbf{p}, \mathbf{q}, t) d\mathbf{p} d\mathbf{q} \tag{4.39}$$

$$\mathbf{C} = \int \mathbf{p}\psi(\mathbf{p}, \mathbf{q}, t) d\mathbf{p} \tag{4.40}$$

It is important to note that $\mathbf{C}$ does not vanish in the case of the Bead-Rod model as it does for the purely Rigid-Rod model. The equations that describe how a given flow field affects the orientation functions are then defined below:

$$\frac{D\mathbf{A}}{Dt} = (\mathbf{W} \cdot \mathbf{A} - \mathbf{A} \cdot \mathbf{W}) + (\mathbf{D} \cdot \mathbf{A} + \mathbf{A} \cdot \mathbf{D} - (2\mathbf{D} : \mathbf{A})\mathbf{A}) +$$
$$... \frac{l_B}{2}[\mathbf{Cm} + \mathbf{mC} - 2(\mathbf{m} \cdot \mathbf{C})\mathbf{A}] - 2k[\mathbf{B} - \mathbf{A}tr(\mathbf{B})] \tag{4.41}$$

$$\frac{D\mathbf{B}}{Dt} = (\mathbf{W} \cdot \mathbf{B} - \mathbf{B} \cdot \mathbf{W}) + (\mathbf{D} \cdot \mathbf{B} + \mathbf{B} \cdot \mathbf{D} - (2\mathbf{D} : \mathbf{A})\mathbf{B}) +$$
$$... \frac{l_B}{2}[\mathbf{Cm} + \mathbf{mC} - 2(\mathbf{m} \cdot \mathbf{C})\mathbf{B}] - 2k[\mathbf{A} - \mathbf{B}tr(\mathbf{B})] \tag{4.42}$$

$$\frac{D\mathbf{C}}{Dt} = \nabla\mathbf{v}^t \cdot C - (\mathbf{A} : \nabla\mathbf{v}^t)\mathbf{C} + \frac{l_B}{2}[\mathbf{m} - \mathbf{C}(\mathbf{m} \cdot \mathbf{C})] - k\mathbf{C}[1 - tr(\mathbf{B})] \tag{4.43}$$

$$\mathbf{m} = \frac{\partial^2 v_i}{\partial x_i \partial x_k} A_{jk}\mathbf{e}_i \tag{4.44}$$

As defined earlier, the velocity gradient $\nabla v = \partial v_j / \partial x_i$, and tr() represents the trace of a specified tensor. Because this model accounts only for viscous flow effects, flexibility caused by flow will occur only when second-order spatial derivatives of the velocity term exist in (4.44). As a result, in simple flows, the model does not predict flow induced bending. It has been shown that this theory

exhibits larger flow induced orientation when compared to that of the F-T model [102]. This was said to be a direct cause of the flexibility of the fiber because the flexibility forced the fiber to orient more in the center of the channel flow. Other than this example, the Bead-Rod model has gone unexamined to our knowledge.

4.4.1.2 *Flexible Fiber Kinematics* To simulate perfect flexibility a fiber must be discretized into multiple nodes of junction points, as described above, complicating the use of orientation tensors. Here the common approach is to perform a dynamic simulation of an individual fiber, or multiple fibers within a simulation box. Hinch [91] pioneered the work on flexible fibers by describing the motion of an inextensible but perfectly flexible fiber. To determine an equation of motion for the fiber, a force balance was performed on an infinitely thin thread where the tension forces, T, in the thread were set equal to the viscous forces. This resulted in two equations, one governing the tension within the thread, and the other governing the time rate of change of the position vector $\mathbf{x}(s, t)$ with respect to the arc length s

Evolution equation $\qquad \dot{\mathbf{x}} = \dfrac{\partial \mathbf{x}}{\partial t} = \nabla \mathbf{v} \cdot \mathbf{x} + \dfrac{\partial T}{\partial s} \dfrac{\partial \mathbf{x}}{\partial s} + \dfrac{1}{2} T \dfrac{\partial^2 \mathbf{x}}{\partial s^2} \qquad (4.45)$

Equation for tension $\qquad \dfrac{\partial^2 T}{\partial s^2} - \dfrac{1}{2} \left(\dfrac{\partial^2 \mathbf{x}}{\partial s^2} \right)^2 T = -\dfrac{\partial \mathbf{x}}{\partial t} \cdot \mathbf{D} \cdot \dfrac{\partial \mathbf{x}}{\partial t} \qquad (4.46)$

Equations (4.45) and (4.46) can be solved given the initial fiber orientation and with boundary conditions that the tension is zero at the ends of the thread: $T = 0$ at $s = +/- L$. The theory predicts that the fiber straightens to align itself in the flow direction for simple shear or stretch direction for simple elongation.

4.4.2 Nondilute Suspensions

4.4.2.1 *Theory and Simulations* There is limited literature that attempts to couple a stress to orientation in flexible fiber systems. In what does exist, researchers attempt to extend the use of stress equations based on short fiber theory to flexible systems, more out of convenience than from a theoretical basis. To apply the stress a decision must be made as to how to describe the orientation of a long fiber. For example, some authors have used the end-to-end vector to describe the orientation of long fiber [97]. Other authors have used the tangential orientation of the fiber in combination with direct simulation methods [103].

The GENERIC framework of Grmela [78, 104], which is based on a free energy approach, does allow for the addition of flexibility. Specifically, the GENERIC model uses entropy expressions gained from kinetic theory of polymers and dissipation to phenomenologically describe effects of fiber

flexibility, excluded volume effects, and fiber and polymer mobility. Qualitatively, the model predicts an enhancement in the transient stress overshoot and viscosity with increased flexibility and concentration. In addition, increased flexibility reduces the steady state alignment in the flow direction. Rajabian [78] used this model to simulate the steady state properties of Kevlar fibers in polyethylene and reported it to have good agreement with the viscosity measurements but poor agreement with the first normal stress difference. Further, the model looses accuracy at higher shear rates for both properties. It is also important to note that the accuracy of the orientation model predictions provided by the GENERIC model has not been reported in the literature [78, 104].

Perhaps the first work on nondilute flexible fiber systems was performed by Goddard and Huang [105], who extended the work of Hinch [91] for a noninteracting perfectly flexible fiber. The authors chose to express the viscous drag by a mobility tensor, which can be seen in the following equations

$$\dot{\mathbf{x}} = K_L \left(\frac{\partial T}{\partial s} \right) \frac{\partial \mathbf{x}}{\partial s} + T\mathbf{K}_T \cdot \frac{\partial^2 \mathbf{x}}{\partial s^2} + \nabla \mathbf{v} \cdot \mathbf{x} \tag{4.47}$$

$$K_L \frac{\partial^2 T}{\partial s^2} - \left| \frac{\partial^2 \mathbf{x}}{\partial s^2} \right|^2 K_N T = -\frac{\partial \mathbf{x}}{\partial s} \cdot \nabla \mathbf{v} \cdot \frac{\partial \mathbf{x}}{\partial s} \tag{4.48}$$

where $\mathbf{K}_T$ is the transverse mobility tensor while K_L and K_N are the lateral and normal components of the mobility tensor, respectively, defined by

$$K_L = \frac{\partial \mathbf{x}}{\partial s} \cdot \mathbf{K}_T \cdot \frac{\partial \mathbf{x}}{\partial s} \text{ and, } K_N = \left(\frac{\partial^2 \mathbf{x}}{\partial s^2} \cdot \mathbf{K}_T \cdot \frac{\partial^2 \mathbf{x}}{\partial s^2} \right) \left| \frac{\partial^2 \mathbf{x}}{\partial s^2} \right|^{-2} \tag{4.49}$$

The mobility tensor represents the inverse of the hydrodynamic resistance per unit length. This model has been used to help understand long fiber configuration in a variety of flow fields [106]. However, no attempt was made to associate a stress with the fiber orientation.

Direct simulation methods can be used to track the dynamic behavior of a large number of interacting fibers, and in contrast to continuum simulations, they have the potential to inherently describe very detailed kinematics [72]. Simulations, however, carry a large computational cost. For this reason, direct simulation methods are usually employed to study a specific behavior of a fiber suspension such as lubrication and hydrodynamic forces, and effects of concentration and flexibility [92−94, 107−109]. For example, Skjetne et al. [93] explored a variety of flexible fiber behaviors by modeling the fibers as a connection of prolate spheroids. Similarly, Joung [97] used direct simulations to predict how fiber curvature affected the relative viscosity of a long fiber suspension. They found that even small changes in fiber curvature resulted in large changes in the relative viscosity. Tang and Advani [94] simulated long

fibers in simple shear flow by modeling the fiber as spheres connected by massless rigid rods with ball and socket joints. Their simulations resulted in viscosity predictions between those calculated from transversely isotropic fluid theory and slender body theory [94]. Nevertheless, direct simulations are of great importance in the quest of understanding specific phenomena; however, due to their computational cost they are presently of little use to most commercial processes.

4.4.2.2 Rheological Characterization   Characterizing the rheology of long glass fibers systems poses the same challenges realized by short glass fiber suspensions. However, in many cases the relative ratio of the rheometer geometry to the characteristic length of the fiber is greatly increased. Typically, this complicates measurements to a greater degree than short glass fiber systems. Published experimental literature for long fiber systems is limited but researchers have used rotational equipment, such as parallel-disk ignoring the inhomogeneous shear field, or cone and plate rheometers ignoring the existence of wall boundary effects. In addition to rotational equipment, sliding plate rheometers have shown some effectiveness when dealing with long concentrated fiber systems [110].

Thomasset [111] performed steady-state rheological experiments of glass fiber reinforced polypropylene samples using a parallel-disk rheometer. The authors found a more pronounced yield-like behavior for the long fiber systems than in similar short glass fiber suspensions. Keshtkar et al. [98] and Goto et al. [112] found the steady state viscosity of a fiber suspension to increase with both fiber concentration and flexibility. It was suggested that this was a result of increased likelihood of fiber−fiber interactions. Another interesting characteristic of long fibers reinforced within polymeric melts remains in their ability to flocculate. Keshtkar et al. [98] report that at low shear rates the viscosity of flexible fiber suspensions is quite high, but at high shear rates the viscosity does not depend on the aspect ratio. They attributed this behavior to the notion that flexible fibers may network or flocculate and result in more fiber−fiber contacts at low shear rates, thus enhancing properties [92]. Also significant shear thinning behavior of long fiber suspensions, particularly in the semiconcentrated regime and at low shear rates, is reported in literature [98]. This behavior has also been attributed to floc formation, and fiber−fiber interlocking. Similar flexibility effects are found on the magnitude of the primary normal force, which is found to increase with both fiber concentration and flexibility [13, 88, 98].

The work by Keshtkar et al. [98] is also among one of the very few experiments concerning the stress growth of long fibers using a parallel-disk plate geometry. In their experiments, they showed that in stress growth experiments fiber flexibility enhances both the magnitude and width of the stress overshoot, when plotted with strain. Similar characteristics were reported by Agarwal et al. [113], who used a sliding plate rheometer to analyze the startup rheology of long fiber reinforced polypropylene. Keshtkar et al. [98] ascertain that increased fiber flexibility creates more fiber−fiber interaction than an

equivalent sample made of rigid fibers. Further, in flow reversal experiments Keshtkar et al. [98] report similar effects of flexibility. Specifically, they found that the delayed undershoot started quicker and the magnitude was more pronounced as flexibility increased. In response to this, they suggest that fiber reorientation begins at lower strain values for higher flexible systems, thus causing the longer transient behavior in the stress undershoot measurements. This may be due to lower fiber orientation of the flexible fibers on flow reversal, versus their rigid fiber counterparts. Again, the increase in magnitude of the overshoot is due to higher fiber−fiber interaction.

4.5   CONCLUSIONS

In this chapter we have presented an introduction to the theory for describing the flow behavior and experimental rheology of fiber suspensions. It is without doubt that the flow behavior and associated stresses of these complex fluids are intimately linked to the fiber structure. As such, the numerical treatment of rigid and flexible fiber suspensions is much different in addition to the expected experimental rheology, as currently, little is known. This is a direct result of the stored and released energy by the flexible fibers subject to deformation, and complex fiber configuration.

The theory for rigid fiber suspensions consists of two parts: (1) an equation governing the motion of the fibers and, (2) an equation to calculate the stress. Theoretical treatment for the evolution of fiber orientation has relied on an extension of rigid body theory to a statistical population of like rods. Modification of this theory to extend predictions to nondilute systems has relied on phenomenological expressions, which are able to qualitatively display similar trends to what has been shown experimentally. The equations used to describe the extra stress are less evolved, for concentrated suspensions and are essentially identical to that of dilute suspensions. It is expected that future efforts will be made to include fiber contact to the stress and elucidate the effect of elasticity on non-Newtonian suspending mediums.

Rheological measurements of glass fiber suspensions are complex but have proven to be insightful in understanding the connection between flow and fiber orientation. Specifically, transient shear measurements will likely continue to be a measurement used in the progression of model development as predictions are compared to experiments. In this regard, it cannot be stressed enough that reported measurements should be performed on well-defined suspensions. Furthermore, steady shear measurements of nondilute suspensions should be performed only in rheometric geometries that induce a homogeneous shear field. On a similar topic, the extensional rheology of fiber suspensions is ill defined. This area of research would largely benefit from a well designed series of experiments that accurately characterize the elongational behavior of fiber suspensions. Potentially, this could be accomplished with a lubricated squeeze flow, or semihyperbolic die rheometer [114].

4.6 NOMENCLATURE

$\mathbf{A}$	Second-order orientation tensor
$\mathbf{A}_4$	Fourth-order orientation tensor
a_r	Aspect ratio: defined as the particles (major axis)/(minor axis)
a_{re}	Equivalent aspect ratio
C	Constant for the analytical solution of Jeffery's equation
C''	Shaqfeh and Fredrickson model constant
C_I	Folgar-Tucker constant
c_1	Fiber stress constant in Lipscomb model
$\mathbf{D}$	Rate of strain tensor
d	Fiber diameter
D/Dt	Material derivative
D_r	Rotational diffusion constant
E_Y	Young's modulus
F_z	Normal force
G_v	Phan-Thien and Graham model function
g	Acceleration due to gravity
h	Spacing between fibers
k	Constant for the analytical solution of Jeffery's equation
k_B	Boltzmann's constant
$\mathbf{K}_T$	Transverse mobility tensor
K_L	Lateral component of the mobility tensor
K_N	Normal component of the mobility tensor
L	Fiber length
L_n	Number average fiber length
L_w	Weight average fiber length
M	Ellipsoid major axis or torque
m	Ellipsoid minor axis or extensional flow viscosity constant
m_1, m_2	Fit parameters
N	Hydrodynamic stress constant
N_1	First normal stress difference
N_1^+	First normal stress difference growth function
n	Number of fibers per unit volume
S_m	Average spacing between fibers
T	Period of rotation or tension in Hinch equations
t	Time
t_s	Sedimentation time scale
$\mathbf{u}$	Unit vector used to represent fiber orientation
$\dot{u}$	Material derivative of $\mathbf{u}$
v	Velocity
$\mathbf{W}$	Vorticity tensor
$\mathbf{x}$	Position vector

Greek Symbols

α	Folgar-Tucker constant
γ	Strain
$\dot{\gamma}$	Shear rate
ξ_r	Rotational friction factor
ρ	Density
η	Non-Newtonian steady-state shear viscosity
η_s	Suspending medium viscosity
η^*	Complex viscosity
η^+	Shear stress growth coefficient
η_0	Zero shear viscosity
η_r	Reduced viscosity
$\Delta\eta_r^*$	Reduced complex viscosity
η_{sp}	Specific viscosity
θ	Zenith angle
θ_0	Zenith angle initial condition
$\boldsymbol{\sigma}$	Total stress tensor
$\boldsymbol{\sigma}^+$	Shear stress growth function
$\boldsymbol{\sigma}^-$	Shear stress decay function
$\boldsymbol{\tau}$	Extra stress tensor
$\tau_{critical}$	Shear stress at which a fiber buckles
φ	Azimuthal angle
φ_0	Azimuthal angle initial condition
ϕ	Fiber volume fraction
ψ	Probability distribution function
ω	Frequency
Ω	Constant for D_{ro} equation

DISCLAIMER

Certain commercial materials are identified in this paper to foster understanding. Such identification does not imply recommendation or endorsement by the National Institute of Standards and Technology, nor does it imply that the materials or equipment identified are necessarily the best available for the purpose.

REFERENCES

1. A.P.R. Eberle et al., *Ind. Eng. Chem. Res*, 47, 3470−3488 (2008).
2. M.A. Zirnsak et al., *J. Non-Newt. Fluid Mech.*, 54, 153−193 (1994).
3. R.G. Larson, *The Strucuture and Rheology of Complex Fluids*, Oxford University Press, New York, 1999.

4. D.H. Chung and T.H. Kwon, *Korean-Australian Rheol. J.*, 14, 175−188 (2002).

5. S.G. Advani and C.L. Tucker, *J. Rheol.*, 31, 751−784 (1987).

6. C.J.S. Petrie, *J. Non-Newt. Fluid Mech.*, 87, 369−402 (1999).

7. J.M. Dealy, *J. Rheol.*, 39, 253−265 (1995).

8. M. Chaouche and D.L. Koch, *J. Rheol.*, 45, 369−382 (2001).

9. M. Doi and S.F. Edwards, *The Theory of Polymer Dynamics*, Oxford University Press, New York, 1988.

10. J.M. Burgers, *Kon. Ned. Akad. Wet. Verhand (Erste Sectie)*, 16, 113−184 (1938).

11. G.K. Batchelor, *J. Fluid Mech.*, 46, 813−829 (1971).

12. M. Doi and N.Y. Kuzuu, *J. Poly. Sci. Part B, Polym. Phys.*, 18, 409−419 (1980).

13. L.H. Switzer and D.J. Klingenberg, *J. Rheol.*, 47, 759−778 (2003).

14. M.W. Darlington and G.R. Smith, *Polymer*, 16, 495−462 (1975).

15. M.W. Darlington, *J. Mat. Sci.*, 10, 906−909 (1975).

16. F. Lisy et al., *J. Appl. Polym. Sci.*, 52, 329−352 (1994).

17. K. Thomas and D.E. Meyer, *Plast. Rubber Compos. Process. Appl.*, 1, 35−36 (1976).

18. A. Mavrich et al., *J. Adhesion*, 46, 91−102 (1994).

19. A. Kriete, *Visualization in Biomedical Microscopies—3D Imaging and Computer Applications*, VCH Publishers, New York, 1992.

20. P.J. Hine et al., *Comp. Sci. Tech.*, 53, 125−131 (1993).

21. A.R. Clarke et al., *Comp. Sci. Tech.*, 55, 75−91 (1995).

22. P.J. Hine and R.A. Duckett, *Polym. Compos.*, 25, 237−254 (2004).

23. A.R. Clarke et al., *J. Microscopy—Oxford*, 69−79 (1993).

24. G. Fischer and P. Eyerer, *Polym. Compos.*, 9, 297−304 (1988).

25. Y.H. Lee *et al.*, *Mater. Res. Innov.*, 6, 65−72 (2002).

26. A.P.R. Eberle et al., *J. Non-Newt. Fluid Mech.*, 165, 110−119 (2010).

27. R.S. Bay and C.L. Tucker, *Polym. Eng. Sci.*, 32, 240−253 (1992).

28. B. Moginger and P. Eyerer, *Composites*, 22, 394−398 (1991).

29. E. Lefranche et al., *Adv. Polym. Technol.*, 24, 114−131 (2005).

30. C.W. Macosko, *Rheology Principles, Measurements, and Applications*, Wiley-VCH, New York, 1994.

31. M.A. Nawab and S.G. Mason, *J. Phys. Chem.*, 62, 1248−1253 (1958).

32. W.R. Blankeney, *J. Colloid Interface Sci.*, 22, 324 (1966).

33. A. Attanasio et al., *Trans. Soc. Rheol.*, 16, 147−154 (1972).

34. L.A. Utracki, *Two-Phase Polymer Systems*, Oxford University Press, New York, 1991.

35. A.P.R. Eberle et al., *J. Rheol.*, 53, 1049−1068 (2009).

36. A.J. Giacomin et al., *Polym. Eng. Sci.*, 29, 499−504 (1989).

37. G. Segre and A. Silberberg, *J. Fluid Mech.*, 14, 115−135 (1962).

38. G. Segre and A. Silberberg, *J. Fluid Mech.*, 14, 136−157 (1962).

39. G.B. Jeffery, *Proc. R. Soc. Lond. A*, 102, 161−179 (1922).

40. A. Einstein, *Ann. Phys.*, 19, 289−306 (1906).

41. S.E. Barbosa and M.A. Bibbo, *J. Poly. Sci., Part B, Polym. Phys.*, 38, 1788−1799 (2000).

42. K.B. Moses et al., *Rheol. Acta*, 40, 296−306 (2001).
43. F.P. Bretherton, *J. Fluid Mech.*, 14, 284−304 (1962).
44. R.G. Cox, *J. Fluid Mech.*, 45, 625−657 (1971).
45. H. Brenner, *Int. J. Muliphase Flow*, 1, 195−341 (1974).
46. B.J. Trevelyan and S.G. Mason, *J. Colloid Sci.*, 6, 354−367 (1951).
47. R.L. Powell, *J. Stat. Phys.*, 62, 1073−1091 (1990).
48. H. Giesekus, *Rheol. Acta*, 2, 101−112 (1962).
49. H. Giesekus, *Rheol. Acta*, 2, 112−122 (1962).
50. G.L. Hand, *Arch. Rational Mech. Anal.*, 7, 81−86 (1961).
51. S.M. Dinh and R.C. Armstrong, *J. Rheol.*, 28, 207−227 (1984).
52. M. Doi and S.F. Edwards, *The Theory of Polymer Dynamics*, Clarendon Press, Oxford, 1987.
53. E.J. Hinch and L.G. Leal, *J. Fluid Mech.*, 52, 683−712 (1972).
54. G.L. Hand, *J. Fluid Mech.*, 13, 33−62 (1962).
55. E.J. Hinch and L.G. Leal, *J. Fluid Mech.*, 76, 187−208 (1976).
56. D. Barthes-Biesel and A. Acrivos, *Int. J. Muliphase Flow*, 1, 1−24 (1973).
57. S.G. Advani and C.L. Tucker, *J. Rheol.*, 34, 367 (1990).
58. D.H. Chung and T.H. Kwon, *Polym. Compos.*, 22, 636−649 (1999).
59. D.A. Jack and D.E. Smith, *J. Comp. Mat.*, 38, 1851−1871 (2004).
60. G.G. Lipscomb et al., *J. Non-Newt. Fluid Mech.*, 26, 297−325 (1988).
61. M. Sepehr et al., *J. Polym. Eng.*, 24, 579−610 (2004).
62. Y. Ivanov et al., *J. Rheol.*, 26, 213−230 (1982).
63. A. Okagawa et al., *J. Colloid Interface Sci.*, 45, 303 (1973).
64. E. Ganani and R.L. Powell, *J. Compos. Mater*, 19, 194 (1985).
65. Y. Iso et al., *J. Non-Newt. Fluid Mech.*, 62, 115−134 (1996).
66. Y. Iso et al., *J. Non-Newt. Fluid Mech.*, 62, 135−153 (1996).
67. A.P.R. Eberle et al., *J. Rheol.*, 53, 685−705 (2009).
68. E. Ganani and R.L. Powell, *J. Rheol.*, 30, 995−1013 (1986).
69. M.C. Altan, *J. Thermoplast. Compos. Mater.*, 3, 275−313 (1990).
70. F.P. Folgar and C.L. Tucker, *J. Reinf. Plast. Compos.*, 3, 98−119 (1984).
71. R.S. Bay, "Fiber Orientation in Injection Molded Composites: A Comparison of Theory and Experiment," thesis, University of Illinois, Urbana-Champaign, 1991.
72. R.S. Bay and C.L.T. III, *Polym. Compos.*, 13, 332−341 (1992).
73. N. Phan-Thien et al., *J. Non-Newt. Fluid Mech.*, 103, 251−260 (2002).
74. H.M. Huynh, "Improved Fiber Orientation Predictions for Injection-Molded Composites," Master's thesis, University of Illinois, Urbana-Champaign, 2001.
75. M. Sepehr et al., *J. Non-Newt. Fluid Mech.*, 123, 19−32 (2004).
76. J. Wang et al., *J. Rheol.*, 52, 1179−1200 (2008).
77. A. Ramazani et al., *J. Rheol.*, 45, 945−962 (2001).
78. M. Rajabian et al., *Rheol. Acta*, 44, 521−535 (2005).
79. E.S.G. Shaqfeh and G.H. Fredrickson, *Phys. Fluids A*, 2, 7−25 (1990).
80. N. Phan-Thien and A.L. Graham, *Rheol. Acta*, 30, 44−57 (1991).

81. T. Kitano and M. Funabashi, *Rheol. Acta*, 25, 606−617 (1986).

82. A. Ramazani et al., *J. Non-Newt. Fluid Mech.*, 73, 241−260 (1997).

83. J. Azaiez, *J. Non-Newt. Fluid Mech.*, 66, 35−54 (1996).

84. H.M. Laun, *Colloid & Polym. Sci.*, 262, 257−269 (1984).

85. R. Guo et al., *Polym. Eng. Sci.*, 45, 385−399 (2005).

86. A.T. Mutel, "Rheological Behavior and Fiber Orientation in Simple Flow of Glass Fiber Filled Polypropylene Melts," Ph.D. thesis, McGill University, Montreal, Quebec, Canada, 1989.

87. C. Mobuchon et al., *Polym. Comp.*, 26, 247−264 (2005).

88. J. Thomasset et al., *J. Non-Newt. Fluid Mech.*, 125, 25−34 (2005).

89. J.P. Greene and J.O. Wilkes, *Polym. Eng. Sci.*, 35, 1670−1681 (1995).

90. J.K. Kim and J.H. Song, *J. Rheol.*, 41, 1061−1085 (1997).

91. E.J. Hinch, *J. Fluid Mech.*, 74, 317−333 (1976).

92. M. Djalili-Mogaddam and S. Toll, *J. Non-Newt. Fluid Mech*, 132, 73−83 (2005).

93. P. Skjetne et al., *J. Chem. Phys*, 107, 2108−2121 (1997).

94. W.Z. Tang and S.G. Advani, *CMES*, 8, 165−176 (2005).

95. W.P. Cox and E.H. Merz, *J. Polym. Sci.*, 28, 619−622 (1958).

96. A.T. Mutel and M.R. Kamal, *Polym. Compos.*, 5, 29−35 (1984).

97. C.G. Joung et al., *J. Non-Newt. Fluid Mech.*, 102, 1−17 (2002).

98. M. Keshtkar et al., *J. Rheol.*, 53, 631−650 (2009).

99. M. Sepehr et al., *J. Rheol.*, 48, 1023−1048 (2004).

100. M.R. Kamal et al., *Polym. Compos.*, 5, 289−298 (1984).

101. G.B. Weinberger and J.D. Goddard, *Int. J. Multiphase Flow*, 1, 465−486 (1974).

102. U. Strautins and A. Latz, *Rheol. Acta*, 46, 1057−1064 (2007).

103. R.F. Ross and D.J. Klingenberg, *J. Chem. Phys.*, 106, 2949−2960 (1997).

104. M. Grmela et al., *J. Chem. Phys.*, 109, 6973−6981 (1998).

105. J.D. Goddard and Y.-H. Huang, *J. Non-Newt. Fluid Mech.*, 13, 47−62 (1983).

106. R. Balasubramanyam, *Composites*, 20, 14−20 (1989).

107. G. Ausias et al., *J. Non-Newt. Fluid Mech.*, 135, 46−57 (2006).

108. J. Ferec et al., *J. Rheol.*, 53, 49−72 (2009).

109. X.J. Fan et al., *J. Non-Newt. Fluid Mech.*, 74, 113−135 (1998).

110. K.A. Ericsson et al., *Rheol. Acta*, 36, 397−405 (1997).

111. J. Thomasset et al., *J. Non-Newt. Fluid Mech.*, 125, 25−34 (2005).

112. S. Goto et al., *Rheol. Acta*, 25, 246−256 (1986).

113. N. Agarwal, *Transient Rheology of Polymer Melts Containing Long Glass Fibers,* MS thesis, Virginia Tech, Blacksburg, Virginia, USA, 2009.

114. D.G. Baird and I. Huang, *Appl. Rheol.*, 16, 312−320 (2006).